

Magnetized Proto-Neutron Stars: Structure and Stability

Harsh Chandrakar ^{1,*} Aravind Taridalu ^{1,†} Adamu Issifu ^{2,3,‡} T. K. Jha ^{1,§} and Prashant Thakur ^{4,¶}

¹*Department of Physics, BITS-Pilani K. K. Birla Goa Campus, Goa 403726, India*

²*Departamento de Física, Instituto Tecnológico de Aeronáutica,
DCTA, 12228-900, São José dos Campos, SP, Brazil*

³*Laboratório de Computação Científica Avançada e Modelamento (Lab-CCAM)*

⁴*Department of Physics, Yonsei University, Seoul, 03722, South Korea*

This study examines the evolution of global properties of magnetized proto-neutron stars (PNSs) across four key stages: neutrino-trapping, deleptonization, neutrino-transparent, and the formation of a cold, catalyzed neutron star (NS). We perform general relativistic magnetohydrodynamic simulations under strong magnetic fields ($B \sim 10^{17}$ G). The stellar matter is modeled with equations of state (EoS) derived from relativistic mean-field theory, employing density-dependent couplings calibrated by the DDME2 parameterization. We analyze how the gravitational mass, equatorial radius, shape deformation, magnetic flux, and magnetic-to-binding energy ratio evolve in response to changes in the internal composition, thermodynamic conditions, and magnetic field configuration. Our results show that as PNSs evolve, increasing entropy per baryon and decreasing lepton fractions lead to higher core temperatures. These thermodynamic changes enhance the star's susceptibility to magnetic field-induced deformation, facilitate greater magnetic flux confinement, and increase the magnetic-to-binding energy ratio, especially during the deleptonization and neutrino-transparent phases. The PNS's core temperature also determines the efficiency of the magnetic field decay. We find that dissipation is fastest during the deleptonization and neutrino-transparent phases, a process that ultimately defines the observable magnetic field of the mature NS.

I. INTRODUCTION

The ultra-compact remnants of massive stellar explosions, known as NSs, provide special cosmic laboratories for the study of matter at the extremes of gravity and density [1]. These intriguing objects do not form instantly; rather, they emerge from a brief, violent, and thermally dynamic phase, during which the nascent object is referred to as a PNS [2]. Understanding the PNS phase is therefore critical to understanding the final properties of mature NSs [3]. A PNS is born in the immediate aftermath of a core-collapse supernova or a binary neutron star merger. It is characterized by extreme conditions, including very high temperatures that can reach up to 50 MeV in the core and a high entropy per baryon of $s_B \approx 1-2$ [4]. In this hot and dense environment, neutrinos become trapped on dynamical timescales, leading to a large, trapped lepton fraction and a finite neutrino chemical potential [1, 5, 6]. Over a period of approximately 10–20 seconds, the PNS undergoes significant evolution as it cools and deleptonizes, primarily through the diffusion and emission of these trapped neutrinos [7–9]. Despite being a highly dynamic process, a few seconds after the initial core bounce, the PNS evolution enters the Kelvin-Helmholtz phase [2, 10], where it can be reasonably approximated as a sequence of quasi-equilibrium configurations. This evolutionary path, from a hot, lepton-rich object to a cold, catalyzed NS, is governed by a complex

interplay of the strong, weak, electromagnetic, and gravitational forces, and has a profound impact on the star's structure and composition.

Ultrastrong interior magnetic fields, on the order of 10^{18} G, can significantly influence compact stars in two primary ways. First, they interact with the constituent particles inside the star, thereby modifying the Equation of State (EoS) [11–15]. Second, such intense fields alter the energy-momentum tensor [16–20], leading to the breaking of spherical symmetry and consequently affecting the star's external structure. PNSs are expected to harbor powerful magnetic fields, a feature inherited and dramatically amplified from their progenitors [21, 22]. While observations of magnetars suggest surface fields reaching $10^{15}-10^{16}$ G [23, 24], theoretical arguments based on the virial theorem predict that internal fields could be orders of magnitude stronger, potentially reaching $\sim 10^{18}$ G [25–28]. The amplification from a progenitor star's weaker field is thought to occur through two primary mechanisms during the star's violent birth: the conservation of magnetic flux during gravitational collapse [29] and dynamo processes driven by the PNS's convection and differential rotation [30]. Additionally, magnetorotational instabilities (MRIs) may play a role in rapidly amplifying seed magnetic fields [31–34]. Given the star's high conductivity, these intense fields are considered to be “frozen-in” during the short evolutionary timescale of a PNS [35, 36]. Such enormous magnetic fields are not passive components; they fundamentally alter the PNS's structure and composition [37, 38]. The Lorentz force exerted by the field induces a significant deformation of the star, with the geometry of the distortion depending on the field's configuration [19, 39]. A purely poloidal field makes the star oblate (flattened at the poles), while a purely toroidal field results in a prolate (elongated) shape. Crucially, the extent of this deformation is strongly linked to the star's

* p20220023@goa.bits-pilani.ac.in

† p20250061@goa.bits-pilani.ac.in

‡ ai@academico.ufpb.br

§ tkjha@goa.bits-pilani.ac.in

¶ prashantthakur1921@gmail.com

thermal state; a hot PNS is more susceptible to distortion and will display a greater ellipticity than a cold NS for the same magnetic field strength. This deformation has direct observational consequences, as a rotating, deformed star is a potential source of continuous gravitational waves [40–44].

Beyond modifying the static structure, magnetic fields dynamically affect key physical processes that govern the evolution of a PNS. They influence neutrino transport, alter the core’s chemical composition, and affect the development of hydrodynamical instabilities. In particular, strong magnetic fields impact neutrino transport by introducing anisotropies in neutrino-matter interaction cross-sections [45, 46]. The likelihood of neutrino scattering or absorption depends on the angle between the neutrino’s trajectory and the magnetic field lines. Such fields can also suppress efficient cooling mechanisms like the Direct Urca process, leading to longer thermal relaxation times. The magnetic pressure reduces the central baryon density, which may delay or inhibit the formation of exotic components like hyperons or deconfined quark matter [47, 48]. Additionally, a strong poloidal field leads to an oblate stellar shape, introducing asymmetries in temperature and composition that can result in anisotropic neutrino emission from the surface [49].

To study magnetic fields in PNSs, one must use the framework of General Relativistic Magnetohydrodynamics (GRMHD) [50–52], which couples fluid dynamics with Maxwell’s and Einstein’s equations. However, evolving the full dynamics of spacetime and matter is computationally expensive. A common and well-justified simplification replaces this dynamic evolution with a sequence of static, quasi-equilibrium configurations. This is valid under strong magnetic fields ($B \gtrsim 10^{14}$ G), where the Alfvén timescale is much shorter than the thermal evolution timescale (~ 10 – 20 s), allowing the field to equilibrate rapidly. The extended Conformally Flat Condition (XCFC) further simplifies the metric by assuming spatial conformal flatness. Codes like XNS 4.0 [53, 54] use this approach to efficiently compute magnetized equilibrium structures in general relativity.

In this study, we have modeled non-rotating PNSs to systematically explore the effects of strong magnetic fields on their global properties across the four key stages of PNS evolution. The main objective is to understand how the internal magnetic field configuration and the evolving EoS interact to influence the structure and deformation of the PNS. By constructing non-rotating models, we are able to isolate magnetic effects without the complicating influence of rotation. This allows us to attribute any observed stellar deformation directly to magnetic pressure and tension, thereby enabling a clearer analysis of magnetic field-induced changes. To ensure a self-consistent comparison across all four evolutionary stages, we fix the baryonic mass of our models at $1.92 M_{\odot}$. This isolates the effects of the evolving EoS, guaranteeing that all variations in the star’s gravitational mass, radius, and deformation are a direct result of changes in its internal thermodynamics and composition. This method elimi-

nates the confounding variables that would arise from comparing different stellar progenitors, thus providing a clean framework for our analysis. Our current approach, therefore, serves as a necessary and well-established step in developing a comprehensive understanding of magnetized PNSs.

Additionally, dividing the evolution of newly formed PNSs into four separate physical regimes—neutrino trapping, deleptonization, neutrino-transparent, and a cold, catalyzed configuration—serves two purposes. First, it allows us to verify our calculated global quantities against well-established models for the initial and final stages, which enhances the trustworthiness of our results. Second, it enables a concentrated examination of the predominantly under-researched function of internal magnetic field geometry during the intermediate stages, especially during the deleptonization and neutrino-transparent phases. This phase-resolved method also helps us separate the effects of changing thermodynamic conditions, like changes in entropy, lepton content, and neutrino opacity, from purely magnetic effects. By keeping the baryonic mass the same at all stages, we make sure that any changes in structure we see, like changes in radius, deformation, and magnetic energy content, are mostly due to the way the EoS and magnetic field configuration change together, not because of differences in total mass or composition.

The structure of this paper is as follows: Section II discusses the microphysical inputs relevant to the evolution of proto-neutron stars. Section III outlines the formalism and implementation of magnetic field effects using the XNS 4.0 code. The results are presented and analyzed in Section IV, followed by the main conclusions and key insights in Section V.

II. MICROPHYSICS

To study the interaction between the hadrons (protons and neutrons), we used the quantum hadrodynamics (QHD) formalism [55], in which the exchange of massive mesons simulates the strong force between them. Considering the massive mesons σ (scalar-isoscalar), ω (vector-isoscalar), and ρ (vector-isovector) mesons, the Lagrangian density that describes the system can be expressed as:

$$\mathcal{L}_H = \sum_{N=p,n} \bar{\psi}_N \left[i\gamma^\mu \partial_\mu - \gamma^0 (g_{\omega N} \omega_0 + g_{\rho N} I_3 \rho_{03}) - (m_N - g_{\sigma N} \sigma_0) \right] \psi_N, \quad (1)$$

$$\mathcal{L}_m = -\frac{1}{2} m_\sigma^2 \sigma_0^2 + \frac{1}{2} m_\omega^2 \omega_0^2 + \frac{1}{2} m_\rho^2 \rho_{03}^2, \quad (2)$$

$$\mathcal{L}_l = \sum_l \bar{\psi}_l (i\gamma^\mu \partial_\mu - m_l) \psi_l, \quad (3)$$

Here, ψ_N denotes the baryonic Dirac field for nucleons, with $m_N = 938$ MeV being the nucleon mass. The meson masses are represented by m_i ($i = \sigma, \omega, \rho$), and g_{iN} are the corresponding nucleon-meson coupling constants.

TABLE I: DDME2 parameters.

meson(i)	$m_i(\text{MeV})$	a_i	b_i	c_i	d_i	$g_{iN}(n_0)$
σ	550.1238	1.3881	1.0943	1.7057	0.4421	10.5396
ω	783	1.3892	0.9240	1.4062	0.4775	13.0189
ρ	763	0.5647	7.3672

$I_3 = \pm 1/2$ denotes the isospin projection of the nucleons. The subscript ‘0’ of the meson fields denotes their mean-field equivalent. The term ψ_l refers to the free lepton field, introduced into the stellar matter to ensure charge neutrality, as NSs are physically observable objects. The leptonic sector includes all relevant leptons present in supernova remnants, namely electrons, electron neutrinos, and muons [2, 4, 56–58]. The model is calibrated using the DDME2 parameterization [59], represented by:

$$g_{iN}(n_B) = g_{iN}(n_0) a_i \frac{1 + b_i(\eta + d_i)^2}{1 + c_i(\eta + d_i)^2}, \quad (4)$$

and

$$g_{\rho N}(n_B) = g_{\rho N}(n_0) \exp[-a_\rho(\eta - 1)]. \quad (5)$$

Where $\eta = n_B/n_0$, with $n_0 = 0.152 \text{ fm}^{-3}$ representing the nuclear saturation density for this parameterization, and n_B being the baryon density. The model parameters (a_i , b_i , c_i , and d_i) are fitted to reproduce experimental bulk nuclear matter properties near n_0 . Further details on the binding energy, incompressibility modulus, symmetry energy, and its slope under this parameterization are given in [60, 61]. The parameters of the model, including the corresponding coupling constants and meson masses, are presented in Table I.

To study the evolutionary stages of PNSs, we assume charge neutrality and β -equilibrium in the stellar matter. The corresponding EoS is determined by solving the energy-momentum conservation equations of Eqs. (1), (2), and (3), i.e. $\mathcal{L} = \mathcal{L}_H + \mathcal{L}_m + \mathcal{L}_l$ [62]. Detailed procedures for calculating the EoS for PNSs within this formalism are provided in Refs. [56, 63, 64]. Additional references for cold NS matter using similar relativistic mean-field approaches with density-dependent couplings can be found in Refs. [60, 65, 66]. The EoS is evaluated for four distinct stages of NS evolution, each characterized by different thermodynamic conditions, following the treatments in Refs. [2, 4, 67]. The first two stages correspond to neutrino-trapped matter: The hot, lepton-rich phase immediately after core collapse, when the NS is born, and the deleptonization phase, which occurs shortly after core bounce as the trapped neutrinos begin to diffuse outward. For these neutrino-trapped stages, the thermodynamic condition is governed by:

$$sT = P + \varepsilon - n_B \mu_B - \mu_{\nu_e} (n_{\nu_e} + n_e), \quad (6)$$

where s is the entropy density, T is the temperature, P is the pressure, ε is the energy density, μ_B is the baryon

chemical potential, μ_{ν_e} is the electron neutrino chemical potential, n_{ν_e} is the neutrino number density, and n_e is the electron number density. The final two stages correspond to neutrino-transparent matter: The early post-neutrino escape phase, where the star begins to cool, and the cold, catalyzed NS phase, representing the star’s long-term equilibrium state [57, 64]. For these neutrino-transparent stages, the thermodynamic condition simplifies to:

$$sT = P + \varepsilon - n_B \mu_B. \quad (7)$$

Therefore, by applying the equations presented above, we can determine the EoS properties and the corresponding temperature distributions of the stellar matter at each evolutionary stage. The primary distinction between the neutrino-trapped and neutrino-transparent stages lies in the role of neutrino pressure: During the neutrino-trapped phases, neutrinos contribute significantly to the pressure, helping to support the star against gravitational collapse. In contrast, once the neutrinos have escaped, this pressure support vanishes, making the star more susceptible to gravity-driven contraction.

III. MODELING PROTO-NEUTRON STARS IN A STRONG MAGNETIC FIELD USING XNS 4.0

We investigate the equilibrium configurations of static, axisymmetric, and strongly magnetized PNSs within the framework of general relativity. To model these compact objects, we employ the numerical solver XNS 4.0 [53, 54, 68], which utilizes a simplified version of the 3+1 formalism under the XCFC for the spatial metric [69]. Under XCFC, the spacetime metric takes the form:

$$ds^2 = -\alpha^2 dt^2 + \psi^4 [dr^2 + r^2 d\theta^2 + r^2 \sin^2 \theta (d\phi + \beta^\phi dt)^2] \quad (8)$$

where $\alpha(r, \theta)$ denotes the lapse function, and $\psi(r, \theta)$ is the conformal factor. Einstein’s field equations under this approximation simplify to two elliptic partial differential equations (PDEs) for these metric potentials[70]:

$$\Delta \psi = -2\pi \hat{E} \psi^{-3}, \quad (9)$$

$$\Delta(\alpha\psi) = 2\pi(\hat{E} + 2\hat{S})\psi^{-2}(\alpha\psi) \quad (10)$$

where Δ represents the flat-space Laplacian operator, and \hat{E} and \hat{S} are the rescaled energy and stress source terms, respectively.

To solve the Einstein field equations in the presence of strong magnetic fields, XNS employ the XCFC formalism. This approach simplifies the equations into a tractable set of elliptic partial differential equations, allowing the construction of fully non-perturbative equilibrium solutions. The XCFC method offers significant advantages in terms of numerical stability and computational efficiency. When compared to exact solutions of the full Einstein equations, the XCFC formalism achieves a practical balance between accuracy and computational feasibility [54, 69]. As such,

it provides a reliable framework for systematically studying the structural effects of intense magnetic fields in neutron stars.

The equilibrium structure under ideal magnetohydrodynamic (MHD) conditions with a poloidal magnetic field, described by the magnetic flux function A_ϕ , is governed by the Grad-Shafranov (GS) equation [53, 71]:

$$\tilde{\Delta}_3 \tilde{A}_\phi + \frac{\partial A_\phi}{r \sin \theta} \frac{\partial \ln(\alpha \psi^{-2})}{\partial \ln(\alpha \psi^{-2})} + \psi^8 r \sin \theta \left(\rho h \frac{d\mathcal{M}}{dA_\phi} + \frac{\mathcal{I}}{\bar{\omega}^2} \frac{d\mathcal{I}}{dA_\phi} \right) = 0 \quad (11)$$

where $\tilde{\Delta}_3$ denotes the Grad-Shafranov operator [53], ρ is the rest-mass density, and h is the specific enthalpy. The local enthalpy at any point inside the star is related to the central enthalpy h_c through the relativistic Bernoulli integral:

$$\ln \frac{h}{h_c} + \ln \frac{\alpha}{\alpha_c} - \mathcal{M}(A_\phi) = 0. \quad (12)$$

The functions $\mathcal{M}(A_\phi)$ (the magnetization function) and $\mathcal{I}(A_\phi)$ —where $B_\phi = \alpha^{-1} \mathcal{I}(A_\phi)$ —are arbitrary but must remain constant along magnetic flux surfaces. These free functions determine the magnetic field geometry within the star. In our modeling, we select the forms of \mathcal{M} and \mathcal{I} to ensure the magnetic field remains fully confined within the neutron star and exhibits symmetry about its equatorial plane.

III.0.1. Poloidal and Mixed ("Twisted Torus") Configurations

For stellar models incorporating a poloidal magnetic field along with an additional toroidal component in a twisted torus configuration, the poloidal magnetization function $\mathcal{M}(A_\phi)$ is defined as [72]:

$$\mathcal{M}(A_\phi) = k_{\text{pol}} \left(A_\phi + \frac{1}{2} \xi A_\phi^2 \right), \quad (13)$$

where k_{pol} is the poloidal magnetization constant, and ξ governs the nonlinear contribution to the poloidal field. The toroidal current function $\mathcal{I}(A_\phi)$ is given by:

$$\mathcal{I}(A_\phi) = \frac{a}{\zeta + 1} \Theta[A_\phi - A_\phi^{\text{max}}] (A_\phi - A_\phi^{\text{max}})^{\zeta+1}, \quad (14)$$

with a the twisted torus magnetization constant, ζ the corresponding index, and $\Theta[\cdot]$ the Heaviside step function. The quantity A_ϕ^{max} denotes the maximum value of the vector potential.

In our analysis of purely poloidal field configurations, we set both $a = 0$ and $\xi = 0$, thereby restricting the current structure to a linear form: $J^\phi = \rho h k_{\text{pol}}$. Under these constraints, we constructed two sequences of PNSs, each featuring a purely poloidal magnetic field with a strength

on the order of 10^{17} G. The first sequence explored the full range of stable gravitational masses permitted by four different equations of state (EoSs). The second sequence was generated by varying k_{pol} while holding the baryonic mass fixed at $1.92 M_\odot$ and maximum magnetic field strength $B_{\text{max}} = 5.67 \times 10^{17}$ G.

For mixed-field configurations, we adopted the same functional form for $\mathcal{M}(A_\phi)$, with the nonlinear term again set to $\xi = 0$. The toroidal field component was introduced via the current function $\mathcal{I}(A_\phi)$, this time using a nonzero value of a and setting $\zeta = 0$. Our study systematically examined the influence of varying a and k_{pol} on global stellar properties, across different EoSs, while maintaining a fixed baryonic mass of $1.92 M_\odot$.

III.0.2. Purely Toroidal Configurations

In the case of purely toroidal magnetic field configurations, the standard Grad-Shafranov formalism becomes inapplicable due to the fact that $A_\phi = 0$ throughout the star. Instead, the equilibrium structure is described using functions of the scalar quantity $G = \rho h \alpha^2 \psi^4 r^2 \sin^2 \theta$. The toroidal magnetic field is expressed as $B_\phi = \alpha^{-1} \mathcal{I}(G)$, where the current function $\mathcal{I}(G)$ is defined as:

$$\mathcal{I}(G) = K_m G^m, \quad (15)$$

$$\text{which leads to } \mathcal{M}(G) = -\frac{m K_m^2}{2m-1} G^{2m-1}. \quad (16)$$

Here, K_m is the toroidal magnetization constant, and m is the magnetization index, typically $m \geq 1$. In this work, we fix $m = 1$ and construct a sequence of equilibrium stellar models for each EoS, covering the complete range of stable gravitational masses allowed by the respective EoSs. From these sequences, we analyze equilibrium configurations to explore the dependence of global stellar properties on the EoS, particularly for models with a fixed baryonic mass of $1.92 M_\odot$ and a maximum internal magnetic field strength of $B_{\text{max}} = 5.67 \times 10^{17}$ G.

IV. RESULTS AND DISCUSSION

In this section, we discuss how intense internal magnetic fields (on the order of 10^{17} G) influence the equilibrium configurations of non-rotating PNSs during their evolutionary phases. The equilibrium configurations were constructed using the XNS 4.0 code. The quasi-equilibrium framework was considered an ideal tool for this investigation because it enables us to systematically isolate and quantify how a star's structural response is influenced by the evolving interaction between its magnetic field and thermodynamic state—particularly entropy per baryon and lepton fraction variations. This approach offers fundamental insights into these critical interactions, which would be obscured by the complexities of time-dependent instabilities found in a full dynamical simulation. Our primary objective is to comprehensively examine how strong

magnetic fields impact key global stellar parameters of evolving PNSs, using the formalism presented in Ref. [19]. These parameters define the macroscopic characteristics of the PNSs [4, 73]. Specifically, we analyze how these global stellar properties depend not only on the magnitude of the internal magnetic field but also on its spatial configuration, encompassing variations in the internal distribution of electric currents and the resulting magnetic field geometry, such as purely poloidal, purely toroidal, or mixed-field arrangements. To capture the evolutionary progression, this analysis is conducted for four distinct stages of the star’s evolution, each corresponding to a particular stage in the thermal and compositional evolution of the PNS. For consistency and comparative purposes, all stellar models are fixed at a baryonic mass of $1.92 M_{\odot}$. The advantage of this approach is that it enables us to trace the evolution of a single star from its birth to maturity. Along the evolutionary path, both the gravitational mass and radius are expected to change due to deleptonization and the heating of stellar matter. The only quantity expected to remain conserved throughout the star’s evolution is the baryon number [2, 74]. Additionally, this mass was selected based on an extensive exploration of sequences of magnetized neutron star configurations obtained by varying the central baryon density across all four stages. The baryonic mass of $1.92 M_{\odot}$ emerged as the optimal choice since it corresponds to the greatest average deformation and most pronounced variations in global stellar quantities across all four stages when subjected to varying magnetic field strengths. Unmagnetized reference configurations with the same baryonic mass of $1.92 M_{\odot}$ were also constructed for each stage, facilitating a clear comparative analysis of the effects induced by magnetic fields.

Figure 1 displays the gravitational mass as a function of radius of PNSs as computed using the general Tolman–Oppenheimer–Volkoff (TOV) equations [81], tracing their evolution from hot, neutrino-rich configurations at birth to the formation of a cold, catalyzed NS configuration several years later. The resulting mass-radius relations from this modeling are compared against observational constraints. The steel-blue shaded region represents the constraints from the binary components of GW170817, corresponding to the 90% (outer contour) and 50% (inner contour) confidence levels (CL). We also include the 1σ (68%) credible intervals derived from the NICER X-ray observations of millisecond pulsars: PSR J0030+0451 (shown in cyan and yellow) [76, 82], and PSR J0740+6620 (in orange and peru) [78, 83]. In addition, the recent NICER mass-radius measurement of PSR J0437–4715 [79] is indicated in lilac. The supernova remnant HESS J1731–347 [84, 85] is shown in brown, with the outer contour representing the 90% CL and the inner contour representing the 50% CL. Further discussion of the thermodynamic conditions governing PNS evolution and their influence on stellar structure can be found in Refs. [2, 56, 86] and references therein.

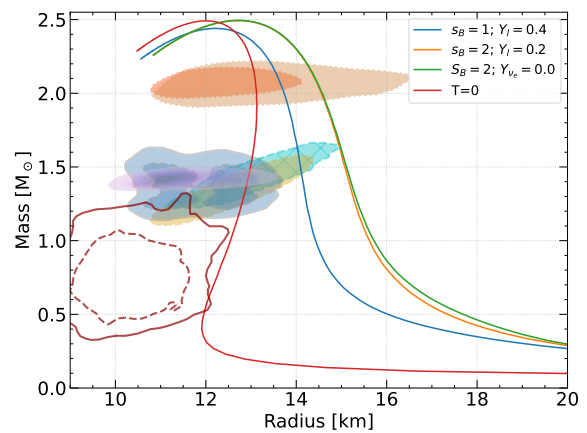


FIG. 1: The plot shows the relationship between the radius and the gravitational mass, M_{\odot} at different stages of PNS evolution, up to the final stage when the star becomes cold and catalyzed at $T = 0$, calculated for unmagnetized case with TOV. The steel blue area indicates the constraints obtained from the binary components of GW170817, with their respective 90% and 50% credible intervals. Additionally, the plot includes the 1σ (68%) CI for the 2D mass-radius posterior distributions of the millisecond pulsars PSR J0030 + 0451 (in cyan and yellow color) [75, 76] and PSR J0740 + 6620 (in orange and peru color)[77, 78], based on NICER X-ray observations. Furthermore, we display the latest NICER measurements for the mass and radius of PSR J0437-4715 [79] (lilac color). The supernova remnant HESS J1731–347 [80] is shown in red, with the outer contour representing the 90% CL and the inner contour representing the 50% CL.

IV.1. PURELY TOROIDAL FIELD

The internal magnetic field structure in magnetized PNSs is governed by the interplay between the magnetization prescription and the EoS. For a purely toroidal configuration, constructed via the functional form of $\mathcal{M}(G)$ in Eq. (16), the EoS dependence is clearly evident. Figure 2 presents isocontours of $|B|$ for equilibrium models at four evolutionary stages, each defined by a distinct EoS: (a) $s_B = 1$, $Y_l = 0.4$; (b) $s_B = 2$, $Y_l = 0.2$; (c) $s_B = 2$, $Y_{\nu_e} = 0$; and (d) $T = 0$. Figure 2 presents meridional cross-sections, where x and z are spatial coordinates in kilometers, illustrating magnetic field surfaces and the distribution of magnetic field strength. The color scale indicates the magnetic field strength in Gauss, with warmer colors (red, yellow) representing higher field strengths and cooler colors (green, blue) denoting lower strengths. The solid cyan line marks the boundary of the magnetized star, while the dashed white line shows the surface of the corresponding unmagnetized star with the same baryonic mass for reference. Comparing the white inner contours of the unmagnetized stars along the evolutionary path, we observe that the size of the star increases from (a) to (c) and then shrinks again at (d). In particular, there is

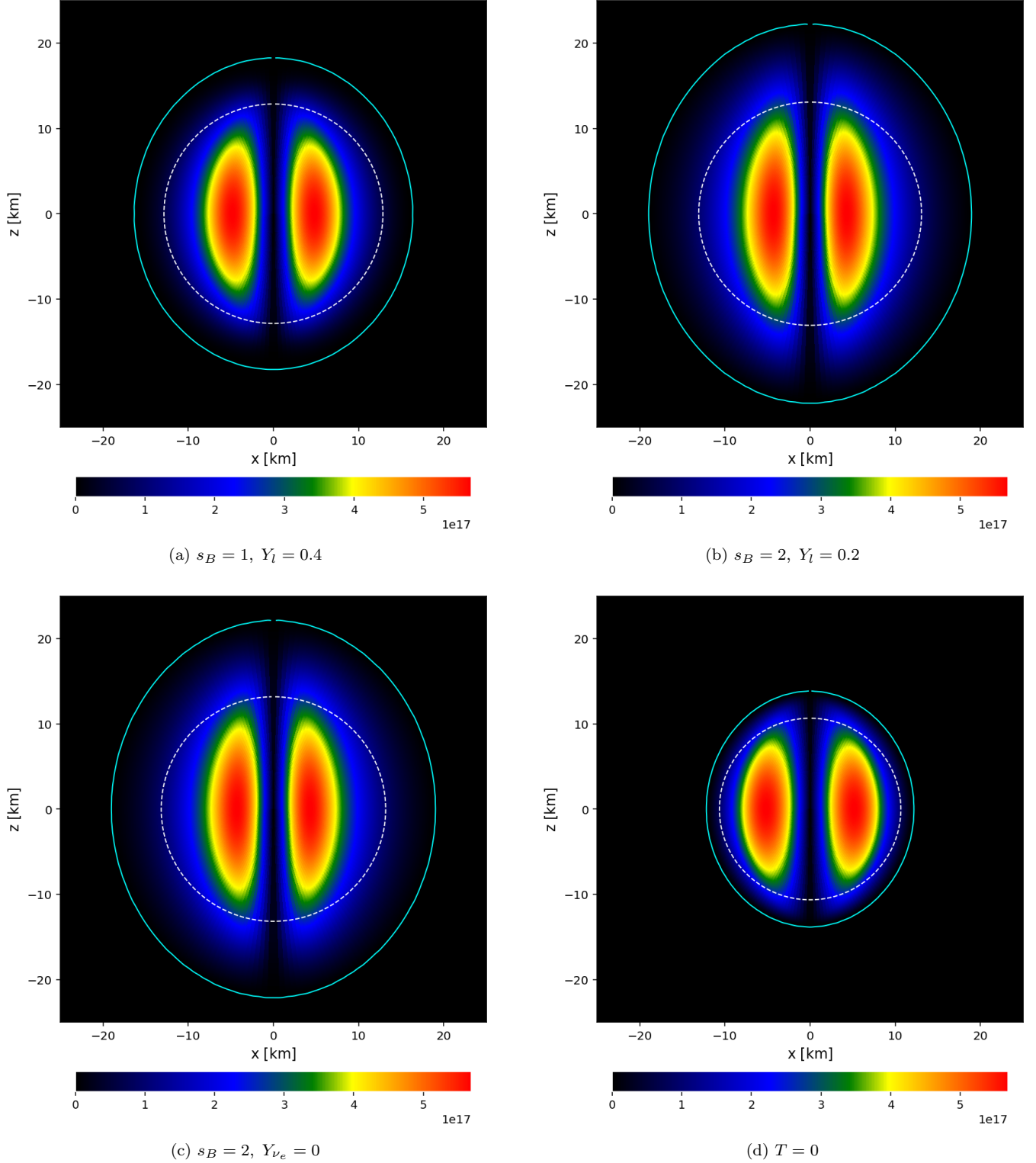


FIG. 2: Meridional cross-sections of PNSs with a purely toroidal magnetic field at four evolutionary stages: (a) neutrino-trapped ($s_B = 1, Y_l = 0.4$), (b) deleptonizing ($s_B = 2, Y_l = 0.2$), (c) neutrino-transparent ($s_B = 2, Y_{\nu_e} = 0$), and (d) cold and catalyzed ($T = 0$). The color map shows the isocontours of magnetic field strength ($|B|$) in Gauss, while the solid cyan and dashed white lines indicate the surfaces of the magnetized and unmagnetized reference stars, respectively. All configurations share the same baryonic mass ($1.92 M_\odot$) and maximum magnetic field ($B_{\max} = 5.67 \times 10^{17}$ G).

TABLE II: Global physical quantities of the equilibrium models with baryonic mass $m_b = 1.92M_\odot$ and maximum magnetic field strength (purely toroidal) $B_{max} = 5.67 \times 10^{17}G$, With ρ_c be the central baryon density, M the gravitational mass, r_e the equatorial radius, r_p the polar radius, R_{circ} the circumferential radius, \bar{e} the deformation parameter, ϕ the magnetic flux, \mathcal{H} the total magnetic energy, \mathcal{W} the binding energy, and T_c the core temperature.

Thermodynamic conditions	ρ_c ($10^{14}g/cm^3$)	M (M_\odot)	r_e (km)	r_p/r_e	R_{circ} (km)	\bar{e} (10^{-1})	ϕ $10^{21}(Wb)$	\mathcal{H}/\mathcal{W} (10^{-1})	T_c (MeV)
$s_B = 1, Y_l = 0.4$	5.88	1.72	16.33	1.12	18.87	-6.03	13.59	1.72	18.88
$s_B = 2, Y_l = 0.2$	5.35	1.75	18.97	1.17	21.49	-9.90	17.53	2.30	43.28
$s_B = 2, Y_{\nu_e} = 0$	5.40	1.74	19.02	1.16	21.56	-9.36	17.25	2.24	44.30
$T = 0$	6.46	1.69	12.17	1.14	14.69	-5.00	11.24	1.41	0.0

a significant increase in size at stages (b) and (c), which corresponds to the deleptonization phase when neutrinos are escaping from the stellar core. During these stages, the core temperature of the PNSs is higher compared to the other stages, as shown in table II. The same table indicates that the intermediate stages are associated with greater \bar{e} , which is also evident from the shape of the outer contours in the figure. Furthermore, comparing stages (a) and (d), \bar{e} is higher in (a), primarily due to the presence of thermal pressure. Thus, a lower T_c , coupled with a higher $c\rho_c$, results in reduced stellar deformation owing to increased compactness and decreased thermal pressure. It is worth mentioning that the ϕ also increases with increasing T_c .

Visually, fig. 3 shows that although all EoSs produce the signature twin off-axis toroidal lobes of maximum magnetic field strength (red regions), the specific field distribution and overall stellar structure are dependent on the thermodynamic conditions of the EoS. The prolate deformation of the magnetized PNS surface relative to its unmagnetized counterpart is evident in all panels. However, the extent of this deformation, as well as the compactness and location of the high-field toroidal regions, varies significantly across the evolutionary stages represented by the different EoSs. Notably, the cold and catalyzed star (panel (d), $T = 0$) appears more compact, with its magnetic field correspondingly confined to a smaller internal volume compared to the hotter, lepton-rich earlier stages at (panels (a)-(b)) and the neutrino transparent stage (panel (c)) this can be attributed to the presence of temperature at these stages that expands the star and reduces its compactness.

All models exhibit a magnetic field distribution characteristic of a purely toroidal configuration: the field strength is null along the symmetry axis, reaches a peak value of $B_{max} = 5.67 \times 10^{17}G$ deep within the stellar core, and gradually decreases to zero at the surface. Despite this common qualitative behavior, notable quantitative differences arise in the structural and global parameters across the various evolutionary phases, as summarized in Table II. Among them, the cold and catalyzed NS ($T = 0$ model) stands out as the most compact. It possesses the highest central baryon density ($\rho_c = 6.46 \times 10^{14}g/cm^3$), the smallest equatorial radius ($r_e = 12.17$ km), and the shortest circumferential radius ($R_{circ} = 14.69$ km). This configuration yields a gravitational mass of $1.69M_\odot$ and displays

a prolate shape, as indicated by a polar-to-equatorial radius ratio of $r_p/r_e = 1.14$ and a deformation parameter of $\bar{e} = -5.00 \times 10^{-1}$. Additionally, it exhibits the lowest magnetic flux ($\phi = 11.24 \times 10^{21}Wb$) and the smallest magnetic-to-binding energy ratio ($\mathcal{H}/\mathcal{W} = 1.41 \times 10^{-1}$).

In contrast to the cold and catalyzed stellar configuration, the earliest evolutionary stage, characterized by $s_B = 1$ and $Y_l = 0.4$ exhibits a notably less compact structure. It has a lower central baryon density of $\rho_c = 5.88 \times 10^{14}g/cm^3$, a larger equatorial radius ($r_e = 16.33$ km), and a greater circumferential radius ($R_{circ} = 18.87$ km). Although its gravitational mass is slightly higher at $1.72M_\odot$, this configuration also displays a more pronounced prolate deformation, with a radius ratio $r_p/r_e = 1.12$ and a deformation parameter of $\bar{e} = -6.03 \times 10^{-1}$. Additionally, it has a higher magnetic flux ($\phi = 13.59 \times 10^{21}Wb$) and a larger $\mathcal{H}/\mathcal{W} = 1.72 \times 10^{-1}$ compared to the $T = 0$ model. These distinctions highlight the impact of thermal and compositional conditions on the global structure and magnetic properties of proto-neutron stars. Even though the first stage is associated with a lower T_c compared to the intermediate stages, it contains a higher neutrino content and is less compact than the cold, compact stellar configuration, as indicated by their ρ_c . These properties influence the star's ability to withstand intense magnetic fields. In particular, by comparing stellar deformation to core temperature in Table II, we can conclude that temperature plays a significant role: the intermediate stages of stellar evolution, which are associated with higher T_c , exhibit greater deformation, as reflected in the higher values of \bar{e} .

Moving to a more evolved but still hot and lepton-rich phase, the configuration with $s_B = 2$ and $Y_l = 0.2$ reveals a further reduction in $\rho_c = 5.35 \times 10^{14}g/cm^3$, accompanied by an increase in $r_e = 18.97$ km and $R_{circ} = 21.49$ km radii. This stage supports a slightly higher gravitational mass of $1.75M_\odot$ and displays the most pronounced prolate deformation across all stages, with a radius ratio $r_p/r_e = 1.17$ and deformation parameter $\bar{e} = -9.90 \times 10^{-1}$. It also possesses the largest magnetic flux ($\phi = 17.53 \times 10^{21}Wb$) and the highest magnetic-to-binding energy ratio ($\mathcal{H}/\mathcal{W} = 2.30 \times 10^{-1}$). The next intermediate state is characterized by $s_B = 2$ after all the neutrinos had escaped from the stellar core, $Y_{\nu_e} = 0$, and it exhibits similar structural properties.

At this stage of the star’s evolution, the temperature of the stellar matter reaches its peak and begin cool with, $\rho_c = 5.40 \times 10^{14} \text{ g/cm}^3$, equatorial radius of 19.02 km and circumferential radius of 21.56 km. The gravitational mass slightly decreases to $1.74 M_\odot$, attributed to the neutrino escape, while the prolate shape remains evident, with $r_p/r_e = 1.16$ and $\bar{e} = -9.36 \times 10^{-1}$. The magnetic flux and energy ratio also remain high, with $\phi = 17.25 \times 10^{21} \text{ Wb}$ and $\mathcal{H}/\mathcal{W} = 2.24 \times 10^{-1}$, respectively. These successive comparisons underscore the trend that, as the PNS evolves thermally and deleptonizes, it progressively contracts, exhibits reduced deformation under (see percentage deformation relative to the cold and catalyzed stellar configuration in Table VII) the same magnetic field generation scheme, and confines less magnetic flux, along with a lower magnetic-to-binding energy ratio for the same peak magnetic field strength due to increased compactness and reduced thermal pressure.

In Table VI, we quantify the structural deformations of PNSs at various evolutionary stages when subjected to a purely toroidal magnetic field. As a reference configuration, we adopt the cold, catalyzed NS at $T = 0$, studied using the same magnetic field generation formalism. This $T = 0$ model, by definition, exhibits zero deformation within our comparative framework and serves as a consistent baseline for evaluating deviations due to thermal and compositional effects. Significant deviations are observed in the first (a) to the third (c) evolutionary stages due to the varied thermodynamic conditions (see references on the study of stellar deformation by magnetic field strength can be found in [87–90]).

For instance, the model with $s_B = 2$ and $Y_{\nu_e} = 0$ shows equatorial, polar, and volumetric deformations of 56.24%, 59.74%, and 290.01%, respectively, relative to the cold NS reference. A similar degree of deformation is seen in the $s_B = 2$, $Y_l = 0.2$ model, with increases of 55.72% (equatorial), 60.26% (polar), and 287.30% (volumetric). Even the first stage considered, $s_B = 1$, $Y_l = 0.4$, exhibits notable deformations of 34.17%, 31.91%, and 138.82%, respectively. These results highlight the critical role of temperature distribution and compactness in determining the extent of magnetic deformation. As shown in table II, the intermediate stages have substantially higher core temperatures than the initial stage, which correlates with the larger deformations observed. This indicates that the star is more susceptible to magnetic distortion during the deleptonization phase than during the neutrino-trapping stage or in the cold, catalyzed NS configuration. Moreover, the results demonstrate that early-stage PNSs, characterized by elevated entropy and lepton content, are significantly larger and more voluminous than their cold counterparts, despite being modeled under the same magnetic field configuration. This underscores the importance of thermal and compositional effects, in conjunction with the equation of state, in shaping the structure and magnetic response of PNSs throughout their evolution [90, 91].

IV.2. PURELY POLOIDAL FIELD

In this section, we examine the influence of a purely poloidal magnetic field configuration on PNSs across different stages of their evolution. For such magnetic field structures, both the stellar equilibrium and the internal field distribution are governed by the choice of the free function $\mathcal{M}(A_\phi)$, defined in Eq. (13). We adopt the linear current approach by setting $\xi = 0$ in this equation, resulting in a poloidal current density given by $J^\phi = \rho h k_{\text{pol}}$. Figure 3 illustrates the magnetic field strength isocontours ($|B|$) for equilibrium PNS configurations at four key evolutionary stages as discussed thoroughly in previous sections. All models in Figure 3 consistently exhibit the expected features of a poloidal magnetic configuration: the magnetic field is strongest at the stellar core (red regions), and the field lines (depicted in white) exhibit a predominantly dipolar structure, extending smoothly through the star and into the surrounding space.

An oblate deformation of the magnetized stellar surface (solid cyan line) relative to the unmagnetized case (dashed white line) is visible in all panels, indicating compression along the magnetic axis and equatorial extension due to magnetic pressure. The degree of this deformation, overall stellar compactness, and the spatial extent of the high-field regions vary across these thermal and compositional stages. Notably, the cold ‘mature’ NS case in panel (d) is substantially more compact, with the strong magnetic field consequently confined to a smaller volume compared to the hotter, PNS stages, and more radially extended PNS configurations shown in panels (a)–(c). The results presented here are qualitatively in agreement with the ones presented in Refs. [19, 90]

The global physical quantities for equilibrium models at different evolutionary stages of a PNS, maintaining a baryonic mass $m_b = 1.92 M_\odot$ and a maximum purely poloidal magnetic field strength $B_{\text{max}} = 5.67 \times 10^{17} \text{ G}$, are detailed in Table III. Among these, the cold stellar configuration (d), representing a late evolutionary stage stands out as the most compact. It possesses the highest central baryon density, $\rho_c = 5.57 \times 10^{14} \text{ g/cm}^3$, the smallest equatorial radius, $r_e = 11.44 \text{ km}$, and the shortest circumferential radius, $R_{\text{circ}} = 14.13 \text{ km}$. This configuration yields a gravitational mass of $1.67 M_\odot$ and displays an oblate shape, as indicated by a polar-to-equatorial radius ratio of $r_p/r_e = 0.78$ and a positive deformation parameter of $\bar{e} = 2.04 \times 10^{-1}$. Additionally, it exhibits the lowest magnetic flux ($\phi = 8.66 \times 10^{21} \text{ Wb}$) and the smallest magnetic-to-binding energy ratio ($\mathcal{H}/\mathcal{W} = 0.77 \times 10^{-1}$).

In contrast to this late-stage, cold configuration, the first evolutionary stages, characterized by $s_B = 1$ and $Y_l = 0.4$, exhibit a notably less compact structure. It has a lower central baryon density of $\rho_c = 4.93 \times 10^{14} \text{ g/cm}^3$, a larger equatorial radius, $r_e = 13.80 \text{ km}$, and a greater circumferential radius, $R_{\text{circ}} = 16.50 \text{ km}$. Its gravitational mass is $1.69 M_\odot$, and this configuration displays a more pronounced oblate deformation compared to the $T = 0$ mode stage, with a radius ratio $r_p/r_e = 0.76$ and a deformation parameter of $\bar{e} = 2.40 \times 10^{-1}$. Furthermore,

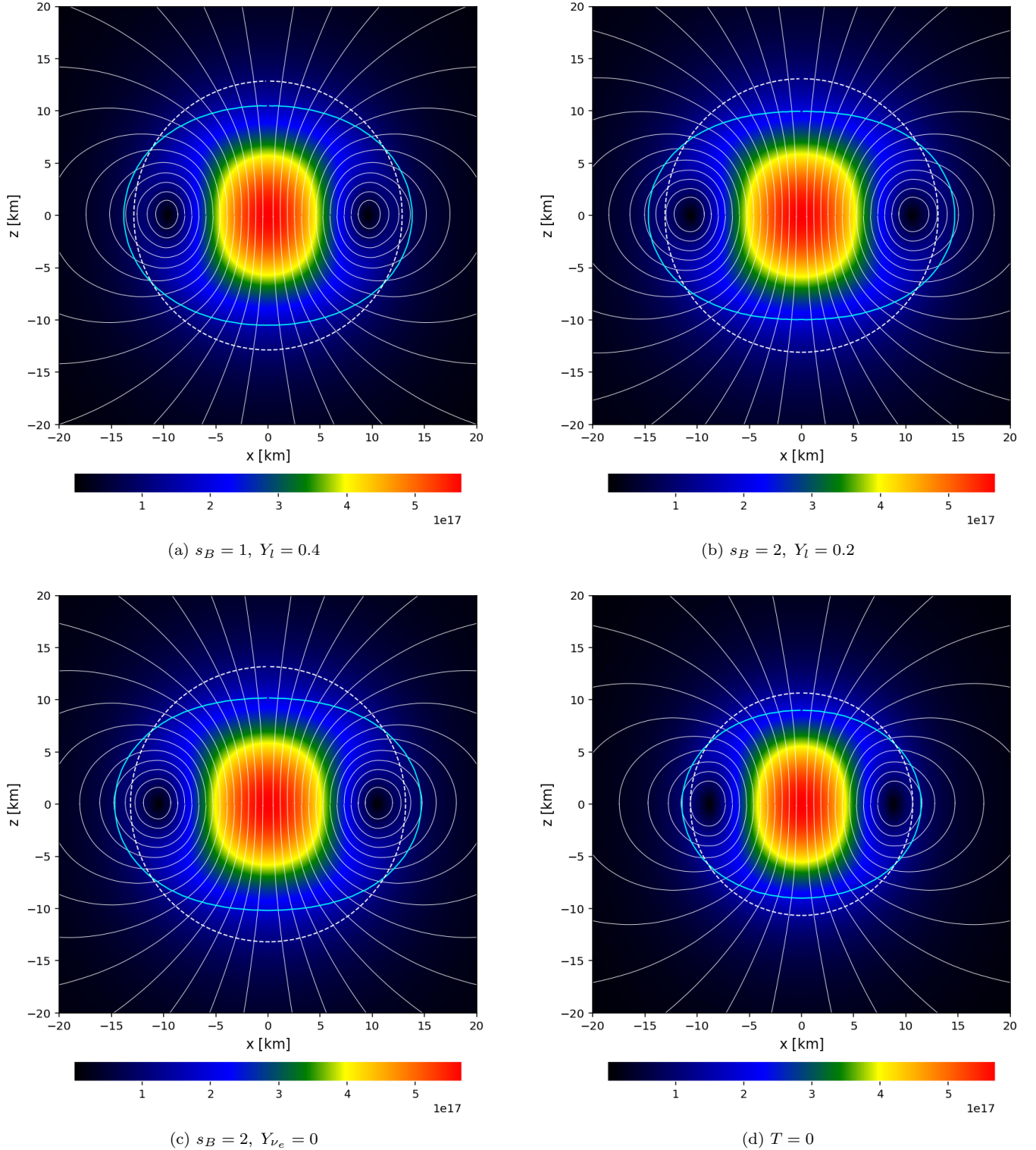


FIG. 3: Meridional cross-sections of PNSs with a purely poloidal magnetic field at four evolutionary stages: (a) neutrino-trapped ($s_B = 1, Y_l = 0.4$), (b) deleptonizing ($s_B = 2, Y_l = 0.2$), (c) neutrino-transparent ($s_B = 2, Y_{\nu_e} = 0$), and (d) cold and catalyzed ($T = 0$). The color map shows the isocontours of magnetic field strength ($|B|$) in Gauss, while the solid cyan and dashed white lines indicate the surfaces of the magnetized and unmagnetized reference stars, respectively. All configurations share the same baryonic mass ($1.92 M_\odot$) and maximum magnetic field ($B_{\max} = 5.67 \times 10^{17}$ G).

TABLE III: Global physical quantities of the equilibrium models with baryonic mass $m_b = 1.92M_\odot$ and maximum magnetic field strength (purely poloidal) $B_{max} = 5.67 \times 10^{17}G$. With ρ_c be the central baryon density, M the gravitational mass, r_e the equatorial radius, r_p the polar radius, R_{circ} the circumferential radius, \bar{e} the deformation parameter, ϕ the magnetic flux, \mathcal{H} the total magnetic energy, \mathcal{W} the binding energy, and T_c the core temperature.

Thermodynamic Condition	ρ_c ($10^{14}g/cm^3$)	M (M_\odot)	r_e (km)	r_p/r_e	R_{circ} (km)	\bar{e} (10^{-1})	ϕ $10^{21}(Wb)$	\mathcal{H}/\mathcal{W} (10^{-1})	T_c (MeV)
$s_B = 1, Y_l = 0.4$	4.93	1.69	13.80	0.76	16.50	2.40	10.38	0.96	16.49
$s_B = 2, Y_l = 0.2$	4.16	1.71	14.66	0.68	17.43	2.91	11.07	1.28	35.83
$s_B = 2, Y_{\nu_e} = 0$	4.26	1.71	14.67	0.69	17.42	2.84	11.06	1.23	37.84
$T = 0$	5.57	1.67	11.44	0.78	14.13	2.04	8.66	0.77	0.0

it has a higher magnetic flux ($\phi = 10.38 \times 10^{21}$ Wb) and a larger magnetic-to-binding energy ratio ($H/W = 0.96 \times 10^{-1}$), alongside a core temperature of 16.49 MeV. These distinctions highlight the impact of thermal evolution on the global structure and magnetic properties under strong poloidal fields.

As the PNS evolves further from the first stage described previously, the configuration with $s_B = 2$ and $Y_l = 0.2$ represents the deleptonization phase. This stage, characterized by a higher core temperature of 35.83 MeV and increased entropy per baryon, reveals a further reduction in central density, $\rho_c = 4.16 \times 10^{14} g/cm^3$, accompanied by a significant increase in equatorial, $r_e = 14.66$ km, and circumferential, $R_{circ} = 17.43$ km, radii. This stage supports a slightly higher gravitational mass of $1.71 M_\odot$ and displays the most pronounced oblate deformation across these stages, with a radius ratio $r_p/r_e = 0.68$ and deformation parameter $\bar{e} = 2.91 \times 10^{-1}$. It also possesses the largest magnetic flux ($\phi = 11.07 \times 10^{21}$ Wb) and the highest magnetic-to-binding energy ratio, $H/W = 1.28 \times 10^{-1}$. These findings underscore the significant role of thermal effects in enhancing both the magnetic flux strength and the resulting stellar deformation during the deleptonization phase.

The third stage, $s_B = 2, Y_{\nu_e} = 0$, exhibits structural properties that are remarkably similar to the preceding $s_B = 2, Y_l = 0.2$ case, yet with subtle distinctions. Its central density, $\rho_c = 4.26 \times 10^{14} g/cm^3$, is marginally higher, while its equatorial radius (14.67 km) and circumferential radius, 17.42 km, are almost identical. The gravitational mass remains the same $1.71 M_\odot$. The oblate deformation, while still pronounced with $r_p/r_e = 0.69$ and $\bar{e} = 2.84 \times 10^{-1}$, is slightly less extreme than in the $Y_l = 0.2$ counterpart. Correspondingly, the magnetic flux ($\phi = 11.06 \times 10^{21}$ Wb) and the magnetic-to-binding energy ratio ($H/W = 1.23 \times 10^{-1}$) are also marginally lower, despite this model achieving the highest core temperature of 37.84 MeV. This stage marks the peak of thermal evolution before the PNS begins to cool and contract toward its final, cold NS state. Both $s_B = 2$ configurations show significantly more extended and deformed structures compared to the first $s_B = 1$ and the last $T = 0$ stages, underscoring a clear trend: as the PNS cools and becomes more compact, magnetic deformation and the relative magnetic energy content gradually diminish.

The data in Table VII demonstrate that PNSs in their

earlier evolutionary phases exhibit substantial structural deviations compared to the compact cold configuration at $T = 0$. For instance, the early evolutionary stage characterized by $s_B = 1$ and $Y_l = 0.4$ show an equatorial radius, $R_e = 13.81$ km, a polar radius $R_p = 10.48$ km, and a volume $V = 8626.74 km^3$. This translates to an equatorial deformation of 20.70%, a polar deformation of 16.76%, and a volumetric deformation of 71.01% relative to the cold stellar configuration. As the star evolves through the deleptonization and neutrino-transparent phases, represented by $s_B = 2, Y_l = 0.2$ or $s_B = 2, Y_{\nu_e} = 0$ respectively, the radii and volume increase further, leading to even more pronounced deformations. Specifically, the $s_B = 2, Y_l = 0.2$ stage exhibits deformations of 28.25% (equatorial), 10.70% (polar), and 87.86% (volumetric). Similarly, the $s_B = 2, Y_{\nu_e} = 0$ stage shows comparable equatorial deformation (28.25%) but a slightly greater polar (13.19%) and volumetric (90.74%) increase relative to the cold stellar reference.

IV.3. MIXED FIELD

Early attempts to model magnetized NSs often employed simplified magnetic field structures—either purely toroidal [92–94] or purely poloidal [16, 95, 96]. However, these idealized field configurations were shown to be dynamically unstable [97–99], a fact originally suggested by Prendergast [100]. More recent simulations have further validated this instability, revealing that magnetic fields with finite helicity naturally evolve toward a stable equilibrium featuring both poloidal and toroidal components [101–103]. These configurations, known as Twisted Torus (TT) structures, exhibit a toroidal component localized in a ring-shaped region beneath the stellar surface and a poloidal component that extends smoothly into the exterior. Motivated by this, this section focuses on such mixed-field geometries. We model the poloidal field using the same free function $\mathcal{M}(A_\phi)$ as in the purely poloidal case (cf. Eq. (13)), but restrict it to a linear form by setting $\xi = 0$. The toroidal field is added through the current function $\mathcal{I}(A_\phi)$, where we similarly use a linear profile by setting $\zeta = 0$ and choosing a nonzero amplitude $a \neq 0$. Although both functions are linear, the inclusion of the toroidal component effectively introduces a nonlinear current structure due to its geometry.

TABLE IV: Global physical quantities of the equilibrium models with baryonic mass $m_b = 1.92M_\odot$, for mixed field configuration with $k_{pol} = 0.2$. With ρ_c be the central baryonic density, M the gravitational mass, r_e the equatorial radius, r_p the polar radius, R_{circ} the circumferential radius, \bar{e} the deformation parameter, ϕ the magnetic flux, \mathcal{H} the total magnetic energy, \mathcal{W} the binding energy, and T_c the core temperature.

Thermodynamic conditions	a	ρ_c (10^{14}g/cm^3)	M (M_\odot)	r_e (km)	r_p/r_e	R_{circ} (km)	\bar{e} (10^{-1})	ϕ $10^{21}(\text{Wb})$	B_c (10^{17}G)	\mathcal{H}/\mathcal{W} (10^{-1})	T_c (MeV)
$s_B = 1, Y_l = 0.4$	0.5	4.95	1.71	14.72	0.73	17.46	2.58	11.83	4.49	1.79	16.55
$s_B = 2, Y_l = 0.2$	0.5	4.44	1.72	15.01	0.74	17.77	2.54	11.06	4.13	1.61	37.65
$s_B = 2, Y_{\nu_e} = 0$	0.5	4.49	1.72	15.21	0.73	17.96	2.58	11.31	4.17	1.67	39.20
$T = 0$	0.5	5.70	1.68	11.47	0.82	14.16	1.77	8.55	4.42	0.93	0.0
$s_B = 1, Y_l = 0.4$	1	5.07	1.70	15.11	0.75	17.80	2.15	10.21	4.08	1.38	16.86
$s_B = 2, Y_l = 0.2$	1	4.40	1.73	16.19	0.68	18.95	2.65	10.81	3.97	1.82	37.39
$s_B = 2, Y_{\nu_e} = 0$	1	4.50	1.72	16.10	0.70	18.83	2.49	10.57	3.93	1.65	39.31
$T = 0$	1	5.51	1.70	12.35	0.72	15.12	2.52	10.19	4.79	1.80	0.0

We perform a systematic parameter study of mixed-field configurations for a fixed baryonic mass of $1.92 M_\odot$. The analysis is divided into two cases, presented in Tables IV and V, to examine the roles of toroidal and poloidal field components separately. In the first case (Table IV), the poloidal magnetization is fixed at $k_{pol} = 0.2$, while the toroidal parameter is varied ($a = 0.5, 1.0$). In the second case (Table V), the toroidal field is held constant at $a = 1.0$, and the poloidal magnetization is varied ($k_{pol} = 0.04, 0.1$). For each magnetic configuration, we calculate the equilibrium properties at four canonical stages of PNS evolution, providing a detailed understanding of how the PNS structure responds to different magnetic field geometries during cooling and deleptonization.

Figure 4 presents the magnetic field strength isocontours ($|B|$) for equilibrium PNS configurations at four key evolutionary stages, as previously discussed. These configurations are computed for a fixed baryonic mass and magnetization parameters ($a = 0.5, k_{pol} = 0.2$). The poloidal magnetic field structure closely follows that seen in purely poloidal models: it permeates the entire PNS, reaches its maximum at the center, and vanishes in a ring-like region along the equatorial plane. Outside the PNS surface, the field transitions smoothly and exhibits a predominantly dipolar structure. In contrast, the toroidal magnetic field shows a distinctly different behavior. It does not occupy the full interior but is instead confined to a toroidal region near the equator, where it attains its peak strength – coinciding with the location where the poloidal component vanishes. This configuration results from the specific choice of the poloidal current distribution and its confinement within the stellar volume. Across all panels, the solid cyan line outlines the oblate deformation of the magnetized PNS surface relative to the unmagnetized case (dashed white line). The thermodynamic and compositional evolution of the PNS directly influences its global structure, modifying its compactness, surface shape, and the spatial extent of strong magnetic fields. In panel (d), the final cold and mature NS is significantly more compact than the hotter PNS stages shown in panels (a) – (c), leading to a more localized confinement of the high-field region.

To examine the structural effects of the toroidal magnetic field component, we compare the equilibrium configurations listed in Table IV for two cases: a moderate toroidal field ($a = 0.5$) and a strong toroidal field ($a = 1.0$), while keeping the poloidal magnetization fixed at $k_{pol} = 0.2$. The impact of increasing toroidal field strength on the stellar structure does not follow a simple monotonic trend but instead exhibits a strong dependence on the PNS evolutionary stage, as discussed in detail below.

At the early, hot, and lepton-rich stage of proto-neutron star evolution ($s_B = 1, Y_l = 0.4$), increasing the toroidal magnetic field strength from $a = 0.5$ to $a = 1.0$ leads to a reduction in stellar oblateness. This is evident from the decrease in the deformation parameter, \bar{e} , from 2.58×10^{-1} to 2.15×10^{-1} , along with a slight increase in the polar-to-equatorial radius ratio (r_p/r_e) from 0.73 to 0.75. The star also becomes more radially extended, with the equatorial radius r_e increasing from 14.72 km to 15.11 km, and the circumferential radius R_{circ} growing from 17.46 km to 17.80 km. This expansion is accompanied by a decrease in the central magnetic field strength, B_c , from 4.49×10^{17} G to 4.08×10^{17} G, and a reduction in the total magnetic flux, ϕ , from 11.83×10^{21} Wb to 10.21×10^{21} Wb. Consequently, the magnetic-to-binding energy ratio, \mathcal{H}/\mathcal{W} , drops from 1.79×10^{-1} to 1.38×10^{-1} . The gravitational mass, M , decreases slightly from $1.71 M_\odot$ to $1.70 M_\odot$, while the central density, ρ_c , and core temperature, T_c , increase marginally.

In a significant departure from the star’s birth, $s_B = 2, Y_l = 0.2$, strengthening the toroidal field during this deleptonizing phase makes the star more oblate. The deformation parameter \bar{e} increases from 2.54×10^{-1} to 2.65×10^{-1} , and the radius ratio r_p/r_e drops sharply from 0.74 to 0.68. This is accompanied by a substantial increase in both the equatorial radius from 15.01 km to 16.19 km and the circumferential radius from 17.77 km to 18.95 km. The central density decreases from $4.44 \times 10^{14} \text{g/cm}^3$ to $4.40 \times 10^{14} \text{g/cm}^3$, while the gravitational mass shows a slight increase from $1.72 M_\odot$ to $1.73 M_\odot$. The core temperature is slightly lower for the stronger field, at 37.39 MeV compared to 37.65 MeV. While the central

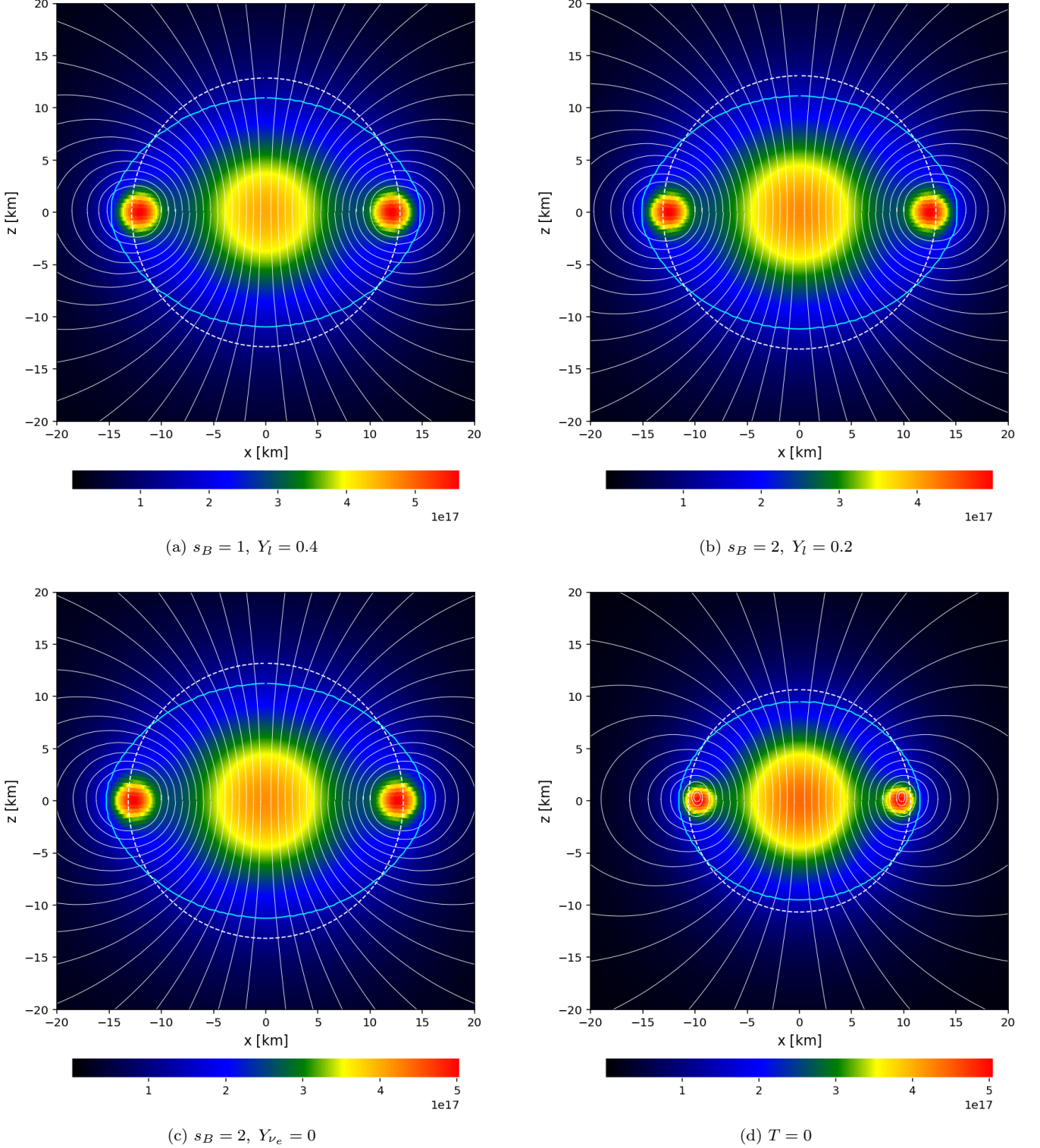


FIG. 4: Meridional cross-sections of PNSs with a mixed magnetic field at four evolutionary stages: (a) neutrino-trapped ($s_B = 1, Y_l = 0.4$), (b) deleptonizing ($s_B = 2, Y_l = 0.2$), (c) neutrino-transparent ($s_B = 2, Y_{\nu_e} = 0$), and (d) cold and catalyzed ($T = 0$). The color map shows the total magnetic field strength ($|B|$) in Gauss and the white lines trace the poloidal magnetic field lines, while the solid cyan and dashed white lines indicate the surfaces of the magnetized and unmagnetized reference stars, respectively. All configurations share the same baryonic mass ($1.92 M_\odot$) and were computed with magnetic parameters $a = 0.5$ and $k_{\text{pol}} = 0.2$.

TABLE V: Global physical quantities of the equilibrium models with baryonic mass $m_b = 1.92M_\odot$, for mixed field configuration with $a = 1.0$. With ρ_c be the central baryon density, M the gravitational mass, r_e the equatorial radius, r_p the polar radius, R_{circ} the circumferential radius, \bar{e} the deformation parameter, ϕ the magnetic flux, \mathcal{H} the total magnetic energy, \mathcal{W} the binding energy, and T_c the core temperature.

Thermodynamic conditions	k_b	ρ_c (10^{14}g/cm^3)	M (M_\odot)	r_e (km)	r_p/r_e	R_{circ} (km)	\bar{e} (10^{-1})	ϕ $10^{21}(\text{Wb})$	B_c (10^{17}G)	\mathcal{H}/\mathcal{W} (10^{-1})	T_c (MeV)
$s_B = 1, Y_l = 0.4$	0.04	5.40	1.67	12.84	0.99	15.43	0.07	1.78	0.78	0.03	17.70
$s_B = 2, Y_l = 0.2$	0.04	4.88	1.68	13.14	0.98	15.74	0.08	1.80	0.75	0.04	40.46
$s_B = 2, Y_{\nu_e} = 0$	0.04	4.95	1.68	13.24	0.98	15.83	0.08	1.79	0.74	0.03	41.84
$T = 0$	0.04	5.91	1.65	10.68	0.99	13.27	0.09	1.85	0.92	0.05	0.0
$s_B = 1, Y_l = 0.4$	0.1	5.46	1.67	13.24	0.94	15.84	0.51	4.70	2.00	0.25	17.84
$s_B = 2, Y_l = 0.2$	0.1	4.95	1.68	13.54	0.93	16.16	0.59	4.85	1.94	0.28	40.87
$s_B = 2, Y_{\nu_e} = 0$	0.1	5.01	1.68	13.63	0.94	16.26	0.57	4.83	1.93	0.27	42.20
$T = 0$	0.1	5.97	1.66	10.98	0.93	13.60	0.60	4.65	2.29	0.30	0.0

field strength and magnetic flux decrease slightly, the overall magnetic energy relative to the binding energy \mathcal{H}/\mathcal{W} increases from 1.61×10^{-1} to 1.82×10^{-1} , indicating a complex redistribution of energy during deleptonization.

At the neutrino-transparent stage, ($s_B = 2, Y_{\nu_e} = 0$), the effects of the toroidal magnetic field resemble those observed at the initial, lepton-rich stage. A stronger toroidal field ($a = 1.0$) again leads to reduced stellar oblateness, with the deformation parameter \bar{e} decreasing from 2.58×10^{-1} to 2.49×10^{-1} . The star remains more radially extended in the presence of the stronger field, with the equatorial radius increasing from 15.21 km ($a = 0.5$) to 16.10 km ($a = 1.0$). In contrast, the gravitational mass and central density show negligible change between the two cases. The core temperature is slightly higher for the stronger field, increasing from 39.20 MeV to 39.31 MeV. Consistent with other hot evolutionary stages, the central magnetic field strength decreases as the toroidal field strengthens, dropping from 4.17×10^{17} G to 3.93×10^{17} G.

The final, cold, Catalyzed NS ($T = 0$) state exhibits the most pronounced and often reversed response to the toroidal field. Here, a stronger toroidal component makes the star more oblate, with the deformation parameter \bar{e} increasing from 1.77×10^{-1} to 2.52×10^{-1} . The star is both more massive ($1.70 M_\odot$ vs. $1.68 M_\odot$) and has a significantly larger equatorial radius (12.35 km vs. 11.47 km). In a key reversal of the trend observed in the hot PNS stages, both the central magnetic field strength and the overall magnetic energy are substantially higher for the stronger toroidal field. B_c increases from 4.42×10^{17} G to 4.79×10^{17} G, and the \mathcal{H}/\mathcal{W} ratio nearly doubles from 0.93×10^{-1} to 1.80×10^{-1} . This highlights that the toroidal field's structural role is fundamentally different and more pronounced in a compact, gravitationally dominated object than in a thermally-supported PNS.

We now turn to the structural impact of the poloidal magnetic field component, with the results presented in Table V. In this analysis, we hold the strong toroidal field constant ($a = 1.0$) and compare models with a weak poloidal magnetization ($k_b = 0.04$) to those with a stronger one ($k_b = 0.1$). Unlike the complex behavior seen when varying the toroidal field, the response to a

stronger poloidal field is consistent across all evolutionary stages.

At birth, ($s_B = 1, Y_l = 0.4$) stage, increasing the poloidal field strength from $k_b = 0.04$ to $k_b = 0.1$ makes the star more oblate. The deformation parameter, \bar{e} , increases by a factor of seven, from a nearly spherical 0.07×10^{-1} to a highly deformed 0.51×10^{-1} . This is mirrored by the radius ratio r_p/r_e dropping from 0.99 to 0.94. The star also becomes slightly larger, with the equatorial radius r_e increasing from 12.84 km to 13.24 km and the circumferential radius R_{circ} growing from 15.43 km to 15.84 km. The central density ρ_c rises from $5.40 \times 10^{14} \text{g/cm}^3$ to $5.46 \times 10^{14} \text{g/cm}^3$, while the gravitational mass M remains unchanged at $1.67 M_\odot$. The core temperature T_c also increases slightly from 17.70 MeV to 17.84 MeV. As expected, all magnetic quantities increase substantially: the total magnetic flux ϕ rises from 1.78×10^{21} Wb to 4.70×10^{21} Wb, the central field B_c increases from 0.78×10^{17} G to 2.00×10^{17} G, and the magnetic energy ratio (\mathcal{H}/\mathcal{W}) grows from 0.03×10^{-1} to 0.25×10^{-1} .

This consistent trend continues during the hot deleptonization phase $s_B = 2, Y_l = 0.2$. A stronger poloidal field again produces a significantly more oblate star, with \bar{e} increasing from 0.08×10^{-1} to 0.59×10^{-1} and the radius ratio (r_p/r_e) decreasing from 0.98 to 0.93. The equatorial radius expands from 13.14 km to 13.54 km, and the circumferential radius increases from 15.74 km to 16.16 km. The central density rises from $4.88 \times 10^{14} \text{g/cm}^3$ to $4.95 \times 10^{14} \text{g/cm}^3$, with the gravitational mass remaining constant at $1.68 M_\odot$. The core temperature is also higher for the stronger field, rising from 40.46 MeV to 40.87 MeV. The magnetic properties are again enhanced across the board: ϕ increases from 1.80×10^{21} Wb to 4.85×10^{21} Wb, B_c rises from 0.75×10^{17} G to 1.94×10^{17} G, and the \mathcal{H}/\mathcal{W} ratio increases sevenfold from 0.04×10^{-1} to 0.28×10^{-1} .

The behavior persists in the neutrino-transparent phase ($s_B = 2, Y_{\nu_e} = 0$). Strengthening the poloidal component results in a much more oblate star, with \bar{e} jumping from 0.08×10^{-1} to 0.57×10^{-1} and the radius ratio r_p/r_e dropping from 0.98 to 0.94. The star is slightly larger,

with r_e increasing from 13.24 km to 13.63 km and R_{circ} from 15.83 km to 16.26 km. The central density increases from $4.95 \times 10^{14} \text{ g/cm}^3$ to $5.01 \times 10^{14} \text{ g/cm}^3$ while the mass remains unchanged at $1.68 M_{\odot}$. The core temperature also increases from 41.84 MeV to 42.20 MeV. All magnetic quantities – ϕ , B_c , and \mathcal{H}/\mathcal{W} – show a large and consistent increase, with values for $k_b = 0.1$ being several times larger than those of $k_b = 0.04$, reaffirming the dominant role of the poloidal component.

The final cold, Catalyzed NS state exhibits the same qualitative response. A stronger poloidal field leads to a highly oblate configuration, with \bar{e} increasing from 0.09×10^{-1} to 0.60×10^{-1} and the radius ratio r_p/r_e decreasing from 0.99 to 0.93. The equatorial radius expands from 10.68 km to 10.98 km, and the circumferential radius grows from 13.27 km to 13.60 km. The star is slightly more massive $1.66 M_{\odot}$ vs. $1.65 M_{\odot}$ and has a higher central density $5.97 \times 10^{14} \text{ g/cm}^3$ vs. $5.91 \times 10^{14} \text{ g/cm}^3$. The magnetic properties see the greatest enhancement in this compact state: ϕ increases from $1.85 \times 10^{21} \text{ Wb}$ to $4.65 \times 10^{21} \text{ Wb}$, B_c more than doubles from $0.92 \times 10^{17} \text{ G}$ to $2.29 \times 10^{17} \text{ G}$, and the \mathcal{H}/\mathcal{W} ratio increases from 0.05×10^{-1} to 0.30×10^{-1} . This behavior is physically expected. As the star cools and contracts, as indicated by the decreasing stellar radius relative to hotter stages, magnetic flux conservation ($\phi = B_c \times \text{area}$) requires the central magnetic field B_c to increase to maintain approximately constant magnetic flux [104, 105], as shown in table V. Additionally, in the first stage, when the star is relatively compact due to lower temperature and higher Y_l , we observe higher values of B_c compared to the less compact intermediate stages, when the star remains relatively hotter. This uniform response confirms that the poloidal field is the primary driver of oblateness and magnetic energy in these mixed-field models.

IV.4. Magnetic decay time

The long-term evolution of magnetic fields in PNSs and mature NSs is governed by three primary dissipative processes: Ohmic dissipation, ambipolar diffusion, and Hall drift. The dominant mechanism at any time depends on local conditions such as magnetic field strength, central density, and temperature, with each process characterized by a distinct timescale [106].

The characteristic decay timescale for Ohmic dissipation, τ_{Ohmic} , is given by:

$$t_{\text{Ohmic}} \sim 2 \times 10^{11} \left(\frac{L_5^2}{T_8^2} \right) \left(\frac{\rho}{\rho_{\text{nuc}}} \right)^3 \text{ yr.} \quad (17)$$

The timescale for ambipolar diffusion, $t_{\text{ambipolar}}$, can be expressed as:

$$t_{\text{ambipolar}}^s \sim 3 \times 10^9 \left(\frac{L_5^2 \times T_8^2}{B_{12}^2} \right) \text{ yr,}$$

$$t_{\text{ambipolar}} \sim \frac{5 \times 10^{15}}{T_8^6 \times B_{12}^2} \text{ yr} + t_{\text{ambipolar}}^s, \quad (18)$$

The Hall drift timescale, t_{Hall} , is:

$$t_{\text{Hall}} \sim 5 \times 10^8 \left(\frac{L_5^2}{B_{12}} \right) \left(\frac{\rho}{\rho_{\text{nuc}}} \right) \text{ yr.} \quad (19)$$

Here, L_5 is the characteristic length scale of flux loops in units of 10^5 cm ; T_8 is the core temperature in units of 10^8 K ; and B_{12} is the field strength in units of 10^{12} G . It is important to note that for the ‘cold’ ($T = 0$) model, we use a representative low temperature of 0.1 MeV. This is equivalent to approximately $1.16 \times 10^9 \text{ K}$, corresponding to a value of $T_8 \approx 11.6$ in our calculations. This choice is considered reasonable, as the temperature in cold and catalyzed NS is typically estimated to be $T < 1 \text{ MeV}$ [4]. The dominant magnetic decay mechanism transitions with field strength: from Ohmic decay for weak fields ($B \lesssim 10^{11} \text{ G}$), to Hall drift for intermediate fields ($B \sim 10^{12} - 10^{13} \text{ G}$), and finally to rapid ambipolar diffusion in the strong-field regime ($B \gtrsim 10^{14} \text{ G}$) [106, 107].

The decay of magnetic fields in NS can be studied by solving the decay equation as described in [107],

$$\frac{dB}{dt} = -B(t) \left(\frac{1}{\tau_{\text{ohmic}}} + \frac{1}{\tau_{\text{ambipolar}}} + \frac{1}{\tau_{\text{hall}}} \right) \quad (20)$$

The time evolution of the purely poloidal magnetic field is presented in Figure 5 (top-left panel), with all models initialized at a field strength of $B_{\text{max}} = 5.67 \times 10^{17} \text{ G}$. The results clearly demonstrate that the magnitude of magnetic dissipation over 1000 years is coupled to the star’s thermal state. The decay was most significant in the hot, high-entropy phases ($s_B = 2$); the field in the deleptonization stage decayed to a final value of $3.25 \times 10^{17} \text{ G}$, representing a substantial decay of 42.7%. Similarly, the neutrino-transparent stage showed a significant drop to $3.26 \times 10^{17} \text{ G}$, a reduction of 42.5%. The final cold, catalyzed state exhibited a suppressed decay, with its field only diminishing to $3.69 \times 10^{17} \text{ G}$, a loss of 34.9%. The initial neutrino-trapped stage ($s_B = 1$) displayed an intermediate level of decay, with the field strength falling to $3.48 \times 10^{17} \text{ G}$, a decay of 38.6%. This explicit dependence on the PNS’s thermal properties strongly suggests that temperature-enhanced dissipation mechanisms govern the rapid evolution of the large-scale poloidal field during its first millennium.

The decay of the purely toroidal field, shown in Figure 5 (top-right panel), mirrors the behavior observed in the poloidal case, confirming the role of the star’s thermal state. Starting from the same initial $B_{\text{max}} = 5.67 \times 10^{17} \text{ G}$, the two hottest, high-entropy models ($s_B = 2$) again exhibit the most significant decay. The field in the deleptonization stage decays to $3.58 \times 10^{17} \text{ G}$, a loss of 36.9%, while the neutrino-transparent stage shows a nearly identical reduction to $3.59 \times 10^{17} \text{ G}$, a loss of 36.7%. This contrasts with the initial neutrino-trapped stage ($s_B = 1$), where the field decays to $3.71 \times 10^{17} \text{ G}$, a 34.6% loss, and the final cold, catalyzed star, which shows the

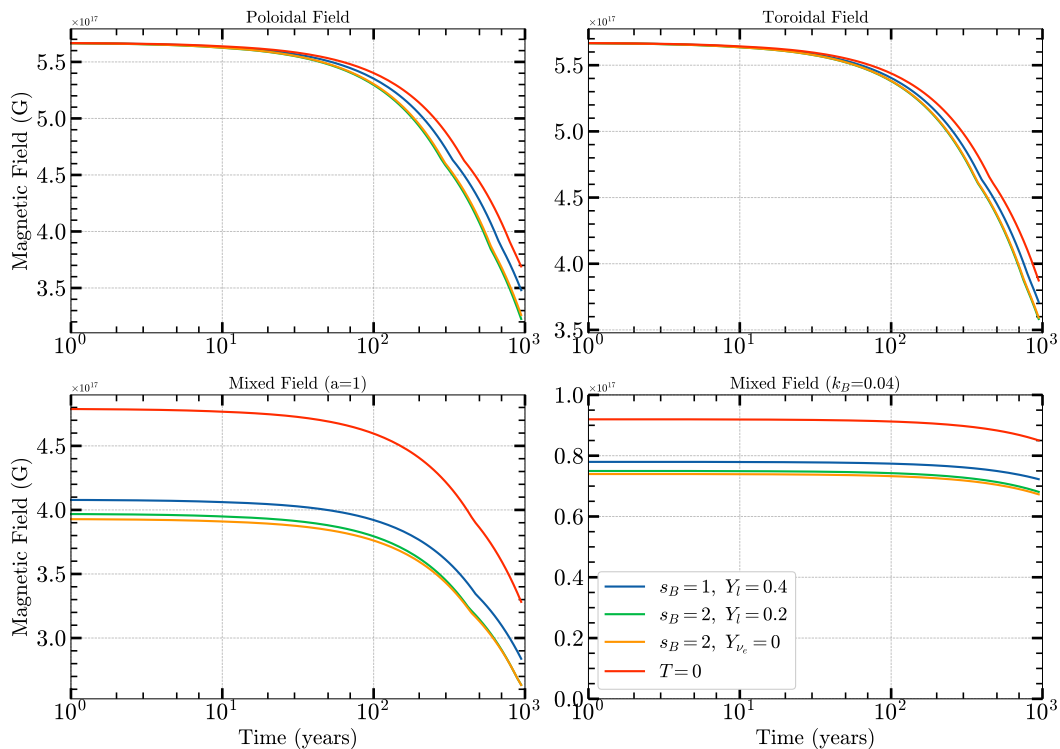


FIG. 5: Time evolution of the maximum magnetic field strength for different magnetic field configurations in PNSs. The upper left and upper right panels show the decay of the poloidal and toroidal magnetic fields, respectively, while the lower panels depict the evolution of mixed field configurations: the lower left for $a = 1$ and the lower right for $k_B = 0.04$. Each curve represents a distinct PNS model: $s_B = 1, Y_l = 0.4$ (blue), $s_B = 2, Y_l = 0.2$ (green), $s_B = 2, Y_{\nu_e} = 0$ (orange), and a cold deleptonized $T = 0$ model (red).

most suppressed decay, with the field only diminishing to $3.87 \times 10^{17} \text{G}$, a of 31.7% loss.

The evolution of a mixed magnetic field, characterized by magnetization parameters ($a = 1, k_{\text{pol}} = 0.2$), is presented in the lower-left panel of Figure 5. A crucial distinction from the pure-field scenarios is that the initial maximum magnetic field strength is now dependent on the thermodynamic state of the PNS itself. Over the 1000-year simulation, the hot, high-entropy phases exhibited the largest relative decay. The deleptonization stage, starting from an initial field of $3.97 \times 10^{17} \text{G}$, decayed to $2.63 \times 10^{17} \text{G}$, a loss of 33.8%. The subsequent neutrino-transparent stage saw its field decline from $3.93 \times 10^{17} \text{G}$ to $2.63 \times 10^{17} \text{G}$, a similar reduction of 33.1%. In contrast, the cold model, despite beginning with the strongest initial field of $4.79 \times 10^{17} \text{G}$, experienced a more moderate relative decay of 31.5%, decaying to $3.28 \times 10^{17} \text{G}$. The initial neutrino-trapped stage displayed the most suppressed relative decay, with its field declining from $4.08 \times 10^{17} \text{G}$ to $2.84 \times 10^{17} \text{G}$, a reduction of only 30.4%. This consistent trend, where the hottest phases show the highest percentage of decay regardless of their initial field strength, reinforces the conclusion that temperature-driven mechanisms are the dominant factor governing the early evolution of complex, mixed-field geometries.

The evolution of the mixed-field configuration with a poloidal constant of $k_B = 0.04$ and toroidal constant

$a = 1$ is depicted in Figure 5. The highest relative decay over 1000 years is again observed in the hot, high-entropy models: the deleptonization stage evolves from an initial $7.50 \times 10^{16} \text{G}$ to $6.81 \times 10^{16} \text{G}$, a 9.2% loss, while the neutrino-transparent stage shows a similar reduction of 9.1% from $7.40 \times 10^{16} \text{G}$ to $6.73 \times 10^{16} \text{G}$. In contrast, the colder models show more suppressed decay. The cold ($T = 0$) model decays by 7.6% from $9.20 \times 10^{16} \text{G}$ to $8.50 \times 10^{16} \text{G}$, while the initial neutrino-trapped stage is the most stable, declining by only 7.3% from $7.80 \times 10^{16} \text{G}$ to $7.23 \times 10^{16} \text{G}$.

V. FINAL REMARKS AND CONCLUSION

In this study, we systematically investigate the structural evolution of strongly magnetized PNSs. We constructed general relativistic equilibrium models for three magnetic configurations, purely toroidal, purely poloidal, and mixed-field. We have traced their evolution across four key thermodynamic stages: neutrino-trapped, deleptonizing, neutrino-transparent, and cold-catalyzed stages. These self-consistent models were generated using the XNS 4.0 code with an EoS derived from the relativistic mean field theory calibrated by the DDME2 parameterization, ensuring both charge neutrality and β -equilibrium throughout the evolution.

Our results demonstrate that a PNS’s structural response to its magnetic field is governed by its thermal and compositional evolution. This effect is most pronounced during the intermediate, high-entropy phases. In these hotter stages, deleptonizing and neutrino-transparent stage, the star’s reduced compactness renders it less rigid and more susceptible to magnetic forces, leading to stronger deformations and more effective flux confinement. The final, cold stage stands in clear contrast, where maximum compactness creates a more rigid star that exhibits minimal deformation and a reduced magnetic energy content.

We find that field geometry plays a decisive role in shaping the star: purely toroidal fields induce prolate deformations, poloidal fields lead to oblate structures, and twisted torus configurations yield stable intermediate responses. Notably, for a fixed baryonic mass of $1.92 M_{\odot}$, the volumetric deformation in a hot PNS can be nearly three times greater than in its cold counterpart under the same toroidal field strength.

In addition, we investigated magnetic field decay mechanisms, including Ohmic dissipation, Hall drift, and ambipolar diffusion. The decay timescales are highly sensitive to core temperature, with hotter phases exhibiting faster field dissipation over typical magnetar lifetimes (approximately 1000 years), regardless of the field geome-

try. This suggests that temperature-enhanced dissipation dominates the early magnetic evolution of NSs.

Overall, this work underscores the interplay between thermodynamics, magnetic topology, and stellar structure from the birth and evolution of magnetized NSs. Accurately modeling PNSs requires capturing both time-dependent thermal evolution and realistic magnetic geometries, as they critically shape key observables such as equatorial radius, central density, deformation parameters, and the long-term evolution of magnetic fields. These insights are crucial for understanding the formation and early evolution of magnetars and may inform future observations related to gravitational wave signals, neutrino emission, and surface temperature distributions from young neutron stars.

ACKNOWLEDGMENTS

A.I. acknowledges financial support from the São Paulo State Research Foundation (FAPESP), Grant No. 2023/09545-1. This work is part of the project INCT-FNA (Proc. No. 464898/2014-5)

VI. APPENDIX

-
- [1] A. Burrows and J. M. Lattimer, *Astrophys. J.* **307**, 178 (1986).
- [2] J. A. Pons, S. Reddy, M. Prakash, J. M. Lattimer, and J. A. Miralles, *Astrophys. J.* **513**, 780 (1999), [arXiv:astro-ph/9807040](#).
- [3] J. M. Lattimer and M. Prakash, *Science* **304**, 536–542 (2004).
- [4] M. Prakash, I. Bombaci, M. Prakash, P. J. Ellis, J. M. Lattimer, and R. Knorren, *Phys. Rept.* **280**, 1–77 (1997), [arXiv:nucl-th/9603042](#).
- [5] H. A. Bethe and J. R. Wilson, *Astrophys. J.* **295**, 14–23 (1985).
- [6] T. J. Mazurek, *Astrophysics and Space Science* **35**, 117–137 (1975).
- [7] W. Keil and H.-T. Janka, *Astronomy and Astrophysics* **296**, 145–+ (1995).
- [8] L. Hüdepohl, B. Müller, H.-T. Janka, A. Marek, and G. G. Raffelt, *Phys. Rev. Lett.* **104**, 251101 (2010).
- [9] L. F. Roberts and S. Reddy, “Neutrino signatures from young neutron stars,” in *Handbook of Supernovae* (Springer International Publishing, 2017) p. 1605–1635.
- [10] T. Fischer, S. C. Whitehouse, A. Mezzacappa, F. K. Thielemann, and M. Liebendorfer, *Astron. Astrophys.* **517**, A80 (2010), [arXiv:0908.1871 \[astro-ph.HE\]](#).
- [11] D. Chatterjee, J. Novak, and M. Oertel, *Eur. Phys. J. A* **57**, 249 (2021), [arXiv:2108.13733 \[nucl-th\]](#).
- [12] D. Chatterjee, T. Elghozi, J. Novak, and M. Oertel, *Mon. Not. Roy. Astron. Soc.* **447**, 3785 (2015), [arXiv:1410.6332 \[astro-ph.HE\]](#).
- [13] I. A. Rather, A. A. Rather, V. Dexheimer, I. Lopes, A. A. Usmani, and S. K. Patra, *Astrophys. J.* **943**, 52 (2023), [arXiv:2209.06016 \[nucl-th\]](#).
- [14] L. Scurto, V. Carvalho, H. Pais, and C. Providência, *Phys. Rev. C* **110**, 045805 (2024), [arXiv:2407.03113 \[nucl-th\]](#).
- [15] T. Malik, D. Sen, T. K. Jha, and H. Mishra, (2018), [arXiv:1811.06258 \[nucl-th\]](#).
- [16] M. Bocquet, S. Bonazzola, E.ourgoulhon, and J. Novak, *Astron. Astrophys.* **301**, 757 (1995), [arXiv:gr-qc/9503044](#).
- [17] C. Y. Cardall, M. Prakash, and J. M. Lattimer, *Astrophys. J.* **554**, 322–339 (2001), [arXiv:astro-ph/0011148](#).
- [18] K. Kiuchi, M. Shibata, and S. Yoshida, *Phys. Rev. D* **78**, 024029 (2008), [arXiv:0805.2712 \[astro-ph\]](#).
- [19] A. Pili, N. Bucciantini, and L. Del Zanna, *Mon. Not. Roy. Astron. Soc.* **439**, 3541–3563 (2014), [arXiv:1401.4308 \[astro-ph.HE\]](#).
- [20] K. Ioka and M. Sasaki, *Astrophys. J.* **600**, 296–316 (2004), [arXiv:astro-ph/0305352](#).
- [21] H. C. Spruit, C. Bassa, Z. Wang, A. Cumming, and V. M. Kaspi, in *AIP Conference Proceedings*, Vol. 983 (AIP, 2008) p. 391–398.
- [22] L. Ferrario, A. Melatos, and J. Zrake, *Space Science Reviews* **191**, 77–109 (2015).
- [23] S. Mereghetti, *The Astronomy and Astrophysics Review* **15**, 225–287 (2008).
- [24] V. M. Kaspi and A. M. Beloborodov, *Annual Review of Astronomy and Astrophysics* **55**, 261–301 (2017), [arXiv:1703.00068 \[astro-ph.HE\]](#).
- [25] E. J. Ferrer, V. de la Incera, J. P. Keith, I. Portillo, and P. L. Springsteen, *Phys. Rev. C* **82**, 065802 (2010).
- [26] D. Lai and S. L. Shapiro, *Astrophys. J.* **383**, 745 (1991).

- [27] I. Fushiki, E. H. Gudmundsson, and C. J. Pethick, *Astrophys. J.* **342**, 958 (1989).
- [28] C. Y. Cardall, M. Prakash, and J. M. Lattimer, *The Astrophysical Journal* **554**, 322–339 (2001).
- [29] L. Woltjer, *Astrophys. J.* **140**, 1309–1313 (1964).
- [30] R. C. Duncan and C. Thompson, *The Astrophysical Journal Letters* **392**, L9 (1992).
- [31] S. Akiyama, J. C. Wheeler, D. L. Meier, and I. Lichtenstadt, *The Astrophysical Journal* **584**, 954 (2003).
- [32] M. Obergaulinger, P. Cerdá-Durán, E. Müller, and M. A. Aloy, *Astronomy & Astrophysics* **498**, 241–271 (2009).
- [33] H. Sawai, S. Yamada, and H. Suzuki, **770**, L19 (2013).
- [34] P. Mösta, C. D. Ott, D. Radice, L. F. Roberts, E. Schnetter, and R. Haas, *Nature* **528**, 376–379 (2015).
- [35] N. Chamel and P. Haensel, *Living Reviews in Relativity* **11** (2008), 10.12942/lrr-2008-10.
- [36] M. G. Alford, A. Schmitt, K. Rajagopal, and T. Schäfer, *Rev. Mod. Phys.* **80**, 1455–1515 (2008).
- [37] J. M. Lattimer and M. Prakash, *The Astrophys. J.* **550**, 426 (2001).
- [38] M. Oertel, M. Hempel, T. Klähn, and S. Typel, *Rev. Mod. Phys.* **89**, 015007 (2017).
- [39] S. Chandrasekhar and E. Fermi, *Astrophys. J.* **118**, 116 (1953).
- [40] L. Gualtieri, R. Ciolfi, and V. Ferrari, *Classical and Quantum Gravity* **28**, 114014 (2011), arXiv:1011.2778 [astro-ph.SR].
- [41] C. Cutler, *Physical Review D* **66** (2002), 10.1103/physrevd.66.084025.
- [42] S. Dall’Osso and L. Stella, *Astrophysics and Space Science* **308**, 119–124 (2007), arXiv:astro-ph/0702075 [astro-ph].
- [43] A. Mastrano, A. Melatos, A. Reisenegger, and T. Akgün, *Monthly Notices of the Royal Astronomical Society* **417**, 2288–2299 (2011), <https://academic.oup.com/mnras/article-pdf/417/3/2288/3826519/mnras0417-2288.pdf>.
- [44] S. Bonazzola and E. Gourgoulhon, “Gravitational waves from neutron stars,” (1996), arXiv:astro-ph/9605187 [astro-ph].
- [45] Y. Luo, S. Zha, and T. Kajino, (2024), arXiv:2405.11555 [astro-ph.HE].
- [46] E. Bauer, J. Torres Patiño, and O. G. Benvenuto, *Phys. Rev. C* **107**, 065804 (2023).
- [47] D. Bandyopadhyay, S. Chakrabarty, and S. Pal, *Phys. Rev. Lett.* **79**, 2176–2179 (1997).
- [48] S. Chakrabarty, *Phys. Rev. D* **54**, 1306–1316 (1996).
- [49] J. F. Pérez-Azorín, J. A. Miralles, and J. A. Pons, *Astronomy & Astrophysics* **451**, 1009–1024 (2006).
- [50] A. Sur, W. Cook, D. Radice, B. Haskell, and S. Bernuzzi, *Mon. Not. Roy. Astron. Soc.* **511**, 3983–3993 (2022), arXiv:2108.11858 [astro-ph.HE].
- [51] P. C.-K. Cheong, A. Tsokaros, M. Ruiz, F. Venturi, J. C. L. Chan, A. K. L. Yip, and K. Uryu, *Phys. Rev. D* **111**, 063030 (2025), arXiv:2409.10508 [astro-ph.HE].
- [52] P. Das, O. Porth, and A. L. Watts, *Mon. Not. Roy. Astron. Soc.* **515**, 3144–3161 (2022), arXiv:2204.00249 [astro-ph.HE].
- [53] N. Bucciantini, A. G. Pili, and L. Del Zanna, *ASP Conf. Ser.* **488**, 211–216 (2014), arXiv:1401.3101 [astro-ph.HE].
- [54] Bucciantini, N. and Del Zanna, L., *A&A* **528**, A101 (2011).
- [55] B. D. Serot and J. D. Walecka, *Int. J. Mod. Phys. E* **6**, 515–631 (1997), arXiv:nucl-th/9701058.
- [56] A. Issifu, K. D. Marquez, M. R. Pelicer, and D. P. Menezes, *Mon. Not. Roy. Astron. Soc.* **522**, 3263–3270 (2023), arXiv:2302.04364 [nucl-th].
- [57] A. Issifu, D. P. Menezes, Z. Rezaei, and T. Frederico, *JCAP* **01**, 024 (2025), arXiv:2405.10386 [nucl-th].
- [58] A. Issifu, F. M. da Silva, and D. P. Menezes, *Eur. Phys. J. C* **84**, 463 (2024), arXiv:2311.12511 [nucl-th].
- [59] G. A. Lalazissis, T. Nikšić, D. Vretenar, and P. Ring, *Phys. Rev. C* **71**, 024312 (2005).
- [60] X. Roca-Maza, X. Vinas, M. Centelles, P. Ring, and P. Schuck, *Phys. Rev. C* **84**, 054309 (2011), [Erratum: *Phys.Rev.C* 93, 069905 (2016)], arXiv:1110.2311 [nucl-th].
- [61] B. T. Reed, F. J. Fattoyev, C. J. Horowitz, and J. Piekarewicz, *Phys. Rev. Lett.* **126**, 172503 (2021), arXiv:2101.03193 [nucl-th].
- [62] D. P. Menezes, *Universe* **7**, 267 (2021), arXiv:2106.09515 [astro-ph.HE].
- [63] A. R. Raduta, M. Oertel, and A. Sedrakian, *Mon. Not. Roy. Astron. Soc.* **499**, 914–931 (2020), arXiv:2008.00213 [nucl-th].
- [64] A. Issifu, P. Thakur, F. M. da Silva, K. D. Marquez, D. P. Menezes, M. Dutra, O. Lourenço, and T. Frederico, *Phys. Rev. D* **111**, 083026 (2025), arXiv:2412.17946 [hep-ph].
- [65] S. Typel, *Particles* **1**, 3–22 (2018).
- [66] T. Nikšić, D. Vretenar, P. Finelli, and P. Ring, *Phys. Rev. C* **66**, 024306 (2002), arXiv:nucl-th/0205009.
- [67] M. Prakash, J. M. Lattimer, J. A. Pons, A. W. Steiner, and S. Reddy, *Lect. Notes Phys.* **578**, 364–423 (2001), arXiv:astro-ph/0012136.
- [68] M. Das and B. Mukhopadhyay, *Astron. Rep.* **67**, S179–S188 (2023).
- [69] I. Cordero-Carrion, P. Cerda-Duran, H. Dimmelmeier, J. L. Jaramillo, J. Novak, and E. Gourgoulhon, *Phys. Rev. D* **79**, 024017 (2009), arXiv:0809.2325 [gr-qc].
- [70] A. G. Pili, N. Bucciantini, and L. Del Zanna, *Monthly Notices of the Royal Astronomical Society* **439**, 3541–3563 (2014), <https://academic.oup.com/mnras/article-pdf/439/4/3541/3981452/stu215.pdf>.
- [71] L. DEL ZANNA, C. Chiuderi, *et al.*, *ASTRONOMY & ASTROPHYSICS* **310**, 341–350 (1996).
- [72] R. Ciolfi, V. Ferrari, L. Gualtieri, and J. A. Pons, *Monthly Notices of the Royal Astronomical Society* **397**, 913–924 (2009).
- [73] H.-T. Janka, K. Langanke, A. Marek, G. Martinez-Pinedo, and B. Mueller, *Phys. Rept.* **442**, 38–74 (2007), arXiv:astro-ph/0612072.
- [74] K. Nakazato and H. Suzuki, *Astrophys. J.* **891**, 156 (2020), arXiv:2002.03300 [astro-ph.HE].
- [75] T. E. Riley *et al.*, *Astrophys. J. Lett.* **887**, L21 (2019), arXiv:1912.05702 [astro-ph.HE].
- [76] M. Miller *et al.*, *Astrophys. J. Lett.* **887**, L24 (2019), arXiv:1912.05705 [astro-ph.HE].
- [77] T. E. Riley *et al.*, *Astrophys. J. Lett.* **918**, L27 (2021), arXiv:2105.06980 [astro-ph.HE].
- [78] M. C. Miller *et al.*, *Astrophys. J. Lett.* **918**, L28 (2021), arXiv:2105.06979 [astro-ph.HE].
- [79] D. Choudhury *et al.*, *The Astrophysical Journal Letters* **971**, L20 (2024).
- [80] V. Doroshenko, V. Suleimanov, G. Pühlhofer, and A. Santangelo, *Nature Astronomy* **6**, 1444–1451 (2022).
- [81] J. R. Oppenheimer and G. M. Volkoff, *Phys. Rev.* **55**, 374–381 (1939).
- [82] T. E. Riley *et al.*, *Astrophys. J. Lett.* **887**, L21 (2019), arXiv:1912.05702 [astro-ph.HE].

- [83] T. E. Riley *et al.*, *Astrophys. J. Lett.* **918**, L27 (2021), [arXiv:2105.06980](https://arxiv.org/abs/2105.06980) [astro-ph.HE].
- [84] V. Doroshenko, V. Suleimanov, G. Pühlhofer, and A. Santangelo, *Nature Astronomy* **6**, 1444–1451 (2022).
- [85] A. Abramowski, F. Acero, F. Aharonian, A. Akhperjanian, G. Anton, A. Balzer, A. Barnacka, U. B. De Almeida, Y. Becherini, J. Becker, *et al.*, *Astronomy & Astrophysics* **531**, A81 (2011).
- [86] G. Malfatti, M. G. Orsaria, G. A. Contrera, F. Weber, and I. F. Ranea-Sandoval, *Phys. Rev. C* **100**, 015803 (2019), [arXiv:1907.06597](https://arxiv.org/abs/1907.06597) [nucl-th].
- [87] A. Colaiuda, V. Ferrari, L. Gualtieri, and J. A. Pons, *Mon. Not. Roy. Astron. Soc.* **385**, 2080–2096 (2008), [arXiv:0712.2162](https://arxiv.org/abs/0712.2162) [astro-ph].
- [88] A. Mastrano, A. G. Suvorov, and A. Melatos, *Mon. Not. Roy. Astron. Soc.* **447**, 3475 (2015), [arXiv:1501.01134](https://arxiv.org/abs/1501.01134) [astro-ph.HE].
- [89] A. Mastrano, P. D. Lasky, and A. Melatos, *Mon. Not. Roy. Astron. Soc.* **434**, 1658 (2013), [arXiv:1306.4503](https://arxiv.org/abs/1306.4503) [astro-ph.HE].
- [90] B. Franzone, V. Dexheimer, and S. Schramm, *Phys. Rev. D* **94**, 044018 (2016), [arXiv:1606.04843](https://arxiv.org/abs/1606.04843) [astro-ph.HE].
- [91] S. K. Lander, P. Haensel, B. Haskell, J. L. Zdunik, and M. Fortin, *Mon. Not. Roy. Astron. Soc.* **503**, 875–895 (2021), [arXiv:2007.14609](https://arxiv.org/abs/2007.14609) [astro-ph.HE].
- [92] K. Kiuchi and S. Yoshida, *Phys. Rev. D* **78**, 044045 (2008).
- [93] K. Kiuchi, K. Kotake, and S. Yoshida, *The Astrophysical Journal* **698**, 541 (2009).
- [94] J. Frieben and L. Rezzolla, *Mon. Not. Roy. Astron. Soc.* **427**, 3406–3426 (2012), [arXiv:1207.4035](https://arxiv.org/abs/1207.4035) [gr-qc].
- [95] K. Konno, *Astron. Astrophys.* **372**, 594 (2001), [arXiv:gr-qc/0105015](https://arxiv.org/abs/gr-qc/0105015).
- [96] S. S. Yazadjiev, *Phys. Rev. D* **85**, 044030 (2012).
- [97] R. J. Tayler, *Monthly Notices of the Royal Astronomical Society* **161**, 365–380 (1973), <https://academic.oup.com/mnras/article-pdf/161/4/365/8076545/mnras161-0365.pdf>.
- [98] G. A. E. Wright, *Monthly Notices of the Royal Astronomical Society* **162**, 339–358 (1973), <https://academic.oup.com/mnras/article-pdf/162/4/339/8073447/mnras162-0339.pdf>.
- [99] P. Markey and R. J. Tayler, *Monthly Notices of the Royal Astronomical Society* **163**, 77–91 (1973), <https://academic.oup.com/mnras/article-pdf/163/1/77/8079493/mnras163-0077.pdf>.
- [100] K. H. Prendergast, *Astrophys. J.* **123**, 498 (1956).
- [101] J. Braithwaite and A. Nordlund, *Astron. Astrophys.* **450**, 1077 (2006), [arXiv:astro-ph/0510316](https://arxiv.org/abs/astro-ph/0510316).
- [102] J. Braithwaite and H. C. Spruit, *Astron. Astrophys.* **450**, 1097 (2006), [arXiv:astro-ph/0510287](https://arxiv.org/abs/astro-ph/0510287).
- [103] J. Braithwaite, *Monthly Notices of the Royal Astronomical Society* **397**, 763–774 (2009), <https://academic.oup.com/mnras/article-pdf/397/2/763/2932157/mnras0397-0763.pdf>.
- [104] D. Lai, *Rev. Mod. Phys.* **73**, 629–662 (2001), [arXiv:astro-ph/0009333](https://arxiv.org/abs/astro-ph/0009333).
- [105] J. M. Lattimer and M. Prakash, *Phys. Rept.* **442**, 109–165 (2007), [arXiv:astro-ph/0612440](https://arxiv.org/abs/astro-ph/0612440).
- [106] P. Goldreich and A. Reisenegger, *ApJ* **395** (1992), 10.1086/171646.
- [107] J. S. Heyl and S. R. Kulkarni, *Astrophys. J. Lett.* **506**, L61 (1998), [arXiv:astro-ph/9807306](https://arxiv.org/abs/astro-ph/9807306).

TABLE VI: In the above table, the equatorial, polar, and volumetric deformations of each of the EoS w.r.t. $T=0$ thermodynamic conditions is calculated in a purely toroidal field configuration.

Thermodynamic conditions	R_e (in km)	R_p (in km)	Volume (km^3)	Equatorial Deformation (in %)	Polar Deformation (in %)	Volumetric Deformation (in %)
$s_B = 1, Y_l = 0.4$	16.33	18.25	20,394.31	34.17	31.91	138.82
$s_B = 2, Y_l = 0.2$	18.96	22.18	33,074.27	55.72	60.26	287.30
$s_B = 2, Y_{\nu_e} = 0$	19.02	22.10	33,305.50	56.24	59.74	290.01
$T = 0$	12.17	13.84	8539.66	0.0	0.0	0.0

TABLE VII: In the above table, the equatorial, polar, and volumetric deformations of each of the EoS w.r.t. $T=0$ thermodynamic conditions is calculated in a purely poloidal field configuration.

Thermodynamic conditions	R_e (in km)	R_p (in km)	Volume (km^3)	Equatorial Deformation (in %)	Polar Deformation (in %)	Volumetric Deformation (in %)
$s_B = 1, Y_l = 0.4$	13.81	10.48	8626.74	20.70	16.76	71.01
$s_B = 2, Y_l = 0.2$	14.67	9.93	9476.52	28.25	10.70	87.86
$s_B = 2, Y_{\nu_e} = 0$	14.67	10.16	9621.82	28.25	13.19	90.74
$T = 0$	11.44	8.97	5044.46	0.0	0.0	0.0

TABLE VIII: In the above table the equatorial, polar and volumetric deformations of each of the EoS w.r.t. $T=0$ thermodynamic conditions is calculated in a mixed field configuration with $a=0.5$.

Thermodynamic conditions	R_e (in km)	R_p (in km)	Volume (km^3)	Equatorial Deformation (in %)	Polar Deformation (in %)	Volumetric Deformation (in %)
$s_B = 1, Y_l = 0.4$	14.72	10.88	9524.03	28.33	15.71	85.19
$s_B = 2, Y_l = 0.2$	15.01	11.07	10,080.16	30.90	17.80	96.00
$s_B = 2, Y_{\nu_e} = 0$	15.21	11.17	10,384.76	32.62	18.85	101.93
$T = 0$	11.47	9.40	5142.85	0.0	0.0	0.0

TABLE IX: In the above table the equatorial, polar and volumetric deformations of each of the EoS w.r.t. $T=0$ thermodynamic conditions is calculated in a mixed field configuration with $a=1.0$.

Thermodynamic conditions	R_e (in km)	R_p (in km)	Volume (km^3)	Equatorial Deformation (in %)	Polar Deformation (in %)	Volumetric Deformation (in %)
$s_B = 1, Y_l = 0.4$	15.11	11.27	9806.35	22.31	26.52	83.22
$s_B = 2, Y_l = 0.2$	16.19	11.07	10,869.36	31.08	24.31	103.08
$s_B = 2, Y_{\nu_e} = 0$	16.10	11.27	11,004.61	30.28	26.52	105.60
$T = 0$	12.35	8.91	5352.34	0.0	0.0	0.0

TABLE X: In the above table the equatorial, polar and volumetric deformations of each of the EoS w.r.t. $T=0$ thermodynamic conditions is calculated in a mixed field configuration with $kb=0.1$.

Thermodynamic conditions	R_e (in km)	R_p (in km)	Volume (km^3)	Equatorial Deformation (in %)	Polar Deformation (in %)	Volumetric Deformation (in %)
$s_B = 1, Y_l = 0.4$	13.24	12.45	9037.24	20.63	21.05	76.03
$s_B = 2, Y_l = 0.2$	13.54	12.65	9530.47	23.32	22.97	85.63
$s_B = 2, Y_{\nu_e} = 0$	13.63	12.75	9780.77	24.22	23.92	90.51
$T = 0$	10.98	10.29	5134.00	0.0	0.0	0.0

TABLE XI: In the above table, the equatorial, polar, and volumetric deformations of each of the EoS w.r.t. $T = 0$ thermodynamic conditions are calculated in a mixed field configuration with $kb = 0.04$.

Thermodynamic conditions	R_e (in km)	R_p (in km)	Volume (km^3)	Equatorial Deformation (in %)	Polar Deformation (in %)	Volumetric Deformation (in %)
$s_B = 1, Y_l = 0.4$	12.85	12.75	8964.95	20.28	20.47	75.62
$s_B = 2, Y_l = 0.2$	13.14	12.95	9451.28	23.04	22.33	85.15
$s_B = 2, Y_{\nu_e} = 0$	13.24	13.04	9646.34	23.96	23.26	88.97
$T = 0$	10.68	10.58	5104.72	0.0	0.0	0.0